Made available by Hasselt University Library in https://documentserver.uhasselt.be

Microtubule-Targeting NAP Peptide-Ru(II)-polypyridyl Conjugate As a Bimodal Therapeutic Agent for Triple Negative Breast Carcinoma

Peer-reviewed author version

CHATTERJEE, Atin; Sarkar, Sandip; Bhattacharjee, Sangheeta; Bhattacharyya, Arpan; Barman, Surajit; Pal, Uttam; Pandey, Raviranjan; ETHIRAJAN, Anitha; Jana, Batakrishna; Das, Benu Brata & Das, Amitava (2024) Microtubule-Targeting NAP Peptide-Ru(II)-polypyridyl Conjugate As a Bimodal Therapeutic Agent for Triple Negative Breast Carcinoma. In: Journal of the American Chemical Society, 147 (1) , p. 532 -547.

DOI: 10.1021/jacs.4c11820
Handle: http://hdl.handle.net/1942/45062

Microtubule-targeting NAP Peptide-Ru(II)-polypyridyl Conjugate as a Bimodal Therapeutic Agent for Triple Negative Breast Carcinoma

Atin Chatterjee,[1,5] Sandip Sarkar,[1] Sangheeta Bhattacharjee,[2#] Arpan Bhattacharyya,[2#] Surajit Barman,[1] Uttam Pal,[3] Raviranjan Pandey,[4] Anitha Ethirajan,*[5,6] Batakrishna Jana,*[1] Benu Brata Das,*[2] Amitava Das*[1]

[1]Department of Chemical Sciences and Center for Advanced Functional Materials Indian Institute of Science Education and Research (IISER) Kolkata, Mohanpur 741246, West Bengal, India.

[2]Laboratory of Molecular Biology, School of Biological Sciences, Indian Association for the Cultivation of Science, Jadavpur, Kolkata 700032, West Bengal, India.

[3]Technical Research Centre, S. N. Bose National Centre for Basic Sciences, Salt Lake, Kolkata 700106, India.

[4]Department of Biological Sciences, Indian Institute of Science Education and Research (IISER) Kolkata, Mohanpur 741246, West Bengal, India.

[5]Hasselt University, Institute for Materials Research (imo-imomec), Nanobiophysics and Soft Matter Interfaces (NSI) group, Martelarenlaan 42, B-3500 Hasselt, Belgium.

[6]imec, imo-imomec, Wetenschapspark 1, B-3590 Diepenbeek, Belgium.

[#]Authors contributed equally.

*Corresponding author. Email: anitha.ethirajan@uhasselt.be , bkjdcs88@iiserkol.ac.in , pcbbd@iacs.res.in , amitava@iiserkol.ac.in

Keywords: Ru-peptide complex, microtubule/tubulin, bimodal therapy, triple negative breast cancer, tumor growth inhibition.

Abstract

Triple-negative breast cancer (TNBC) poses significant treatment challenges due to its high metastasis, heterogeneity, and poor biomarker expression. The N-terminus of an octapeptide NAPVSIPQ (**NAP**) was covalently coupled to a carboxylic acid derivative of $Ru(2,2'\text{-bipy})_3^{2+}$ **(Rubpy)** to synthesize a N-stapled short peptide-Rubpy conjugate (**Ru-NAP**). This photosensitizer (PS) was utilized to treat TNBC through microtubule (MT) targeted chemotherapy and photodynamic therapy (PDT). **Ru-NAP** formed more elaborate molecular aggregates with fibrillar morphology as compared to **NAP**. A much higher binding affinity of **Ru-NAP** over **NAP** towards β-tubulin ($K_{Ru\text{-}NAP}$: $(6.8 \pm 0.55) \times 10^6$ M^{-1}; K_{NAP}: $(8.2 \pm 1.1) \times 10^4$ M^{-1}) was observed due to stronger electrostatic interaction between the MT with an average linear charge density of ~ 85 e/nm and the cationic **Rubpy** part of **Ru-NAP**. This was also supported by docking, simulation and appropriate imaging studies. **Ru-NAP** promoted serum

stability, specific binding of **NAP** to the E-site of the β^{III}-tubulin followed by the disruption of MT network and effective singlet oxygen generation in TNBC cells (MDA-MB-231), causing cell cycle arrest in the G2/M phase and triggering apoptosis. Remarkably, MDA-MB-231 cells were more sensitive to **Ru-NAP** compared to non-cancerous human embryonic kidney (HEK293 cells) when exposed to light ($^{Light}IC_{50}^{Ru\text{-}NAP}$[HEK293]: 17.2 ± 2.5 μM, compared to $^{Light}IC_{50}^{Ru\text{-}NAP}$[MDA-MB-231]: 32.5 ± 7.8 nM, $^{Dark}IC_{50}^{Ru\text{-}NAP}$[HEK293]: > 80 μM, compared to $^{Dark}IC_{50}^{Ru\text{-}NAP}$[MDA-MB-231]: 2.9 ± 0.5 μM). **Ru-NAP** also effectively inhibited tumor growth in MDA-MB-231 xenograft models in nude mice. Our findings provide strong evidence that **Ru-NAP** has a potential therapeutic role in TNBC treatment.

Introduction

Triple-negative breast cancer (TNBC) is a highly metastatic, heterogeneous breast cancer with impaired expression of estrogen (ER), progesterone (PR), and human epidermal growth factor receptor 2 (HER2).[1-2] Poor prognosis and its low response to therapeutics add to therapeutic challenges compared to non-TNBC cases.[3] Recent reports confirm that microtubule (MT) cytoskeleton are validated targets for breast cancer therapy.[4-5] MTs are associated with critical cellular functions including mitosis, cell signaling, intracellular trafficking, and angiogenesis.[6] Any molecule that can modulate the MT dynamics would induce the spindle checkpoint, arresting cell-cycle progression at mitosis with subsequent cell death. MT stabilizers stimulate the assembly of purified tubulin and shift the equilibrium of tubulin polymer from the soluble to the polymerized form.[7-9] This leads to consequential disruption of MT dynamics and mitotic arrest of cancer cells, which has been effectively utilized as a treatment strategy for cancer.[6, 10-12] MTs are present both in interphase cells and dividing cells in mammalian cells. These constitute the highly dynamic mitotic spindle and this accounts for the extreme sensitivity towards therapeutic inhibitors.[6] MT targeting agents (MTAs) are a type of vascular disrupting agents (VDAs).[13] Chemotherapeutic drugs that bind to the colchicine site of tubulin target tumour vasculature to induce blood vessel disruption are used in clinical trials.[14-15] Certain vinca alkaloids and taxanes are part of the FDA-approved drugs for treating haematological malignancies and solid tumours.[16-17] Taxol belongs to taxane family and is being used for treating early-stage, advanced and metastatic breast cancer.[18] A 3.5-Å resolution electron crystallography structure of the tubulin dimer bound to taxol reveals that taxol binds stoichiometrically and specifically to the β-tubulin subunit in MTs.[16] A few of the most recent and effective cancer chemotherapeutic drugs are derived from natural compounds that target

MTs and disrupt the normal function of the mitotic spindle.[19] Site-specific binding of such molecules, either to soluble tubulin or to the MT governs the efficacy of these drugs as chemotherapeutic agents.[11] The major issues that limit the clinical efficacy of taxanes as the MTAs are low solubility and thus bioavailability, a relatively short circulation time $t_{1/2}$ (~ 1 h), inability to cross the blood-brain barrier, high systemic toxicity (e.g. neutropenia, neurotoxicity, genotoxicity, cardiac toxicity, repression of bone marrow, etc.) and the onset of multidrug resistance mechanisms.[18,20] These challenges offer a distinct scope for adopting an alternate strategy in developing MTAs for improved clinical efficacy towards cancer therapy.

NAPVSIPQ (Asn-Ala-Pro-Val-Ser-Ile-Pro-Gln; all amino acids are in L- form) abbreviated as **NAP** is a neuroprotective octapeptide derived from activity-dependent neuroprotective protein (ADNP). Affinity chromatography identified the β^{III}-tubulin as a major **NAP**-binding protein.[21] Presumably, binding of **NAP** to β^{III}-tubulin induces a conformational shift to facilitate tubulin polymerization with the E-site of the β^{III}-tubulin, which is preferentially occupied by Guanosine triphosphate (GTP) rather than Guanosine diphosphate (GDP).[22] As discussed above, MTAs could be a part of the effective strategy for treating breast cancer. TNBC remains a challenging subtype of breast cancer and there is distinct scope to address the unmet needs to improve the outcome of TNBC therapeutics. With this aim, we have used the β^{III}-tubulin-specific binding of **NAP** peptide in demonstrating a proof-of-concept of a microtubule-specific photosensitizer (PS) for the bimodal killing of the TNBC cells using Chromophore Assisted Light Inactivation (CALI) concept.[23,24] Specific binding of the **NAP** peptide conjugated to a substitution inert Ru(II)-polypyridyl moiety (a singlet oxygen ($^1O_2$) initiator) to the cytoskeleton protein allows this conjugate to qualify as CALI-based agent while addressing the limitations of systemic toxicity induced by conventional PDT-agents through indiscriminate intracellular reactive oxygen species (ROS) generation.[25-28] Short lifetime (~ 6 μs) and diffusion length (< 50 nm) for $^1O_2$ in human physiology enable a highly localized spatiotemporal activity to minimize the possibility of indiscriminate systemic toxicity.[24,29-33] Importantly, literature reports suggest that CALI-based PDT agents are rarely exploited for *in vivo* studies.[32,33] Antibody-drug conjugates (ADCs) have also been conceived to achieve organelle/tissue-specific release of cytotoxic drugs to avoid non-specific biodistribution and undesired systemic toxicities. However, the major shortcomings of the first- and second-generation ADCs include the immunogenic responses and fast clearance in circulation, apart from other drug-design issues.[34-38] Arguably, small molecular weight peptide-drug conjugates have the advantages of higher drug loading and enhanced tissue penetration capacity,

degradation without triggering any immunogenic responses in physiology, stability towards proteolysis and facile synthesis.[39-40] Recently, Kornienko, Bonnet and their coworkers have demonstrated the efficacy of photoactivated chemotherapy in A549 xenografts in nude mice through the *in-situ* release of a MT-targeting drug, rigidin.[20]

The PDT efficiency is compromised by the hypoxic feature of tumours, especially for the PDT agents that induce Type II reactions. Here, the triplet state (T_1) of the PS interacts with $^3O_2$ to form $^1O_2$, a potent ROS.[41] Therefore, combining PDT and chemotherapy is crucial to counter balance each other's limitations.[42] Considering this, we have utilized **NAP** peptide conjugated $Ru(2,2´\text{-bipy})_3^{2+}$ (**Rubpy**) derivative (**Ru-NAP)** as a potent bimodal chemotherapeutic and PDT agent for killing TNBC cells (Scheme 1). **Ru-NAP** conjugate is more efficient in stabilizing MT by favouring tubulin polymerization. Live cell microscopy confirms the targeting ability of **Ru-NAP** to the MT in TNBC (MDA-MB-231) cells. Thus, it causes certain toxicity in the dark through the binding of **Ru-NAP** fibers to the tubulin/MT and followed by disruption of the MT network which signifies its' chemotherapeutic effect. Moreover, *in vitro* and intracellular studies confirm that **Ru-NAP** also exhibit superior phototoxicity compared to the individual components, **Rubpy** or **NAP**. The higher toxicity towards live MDA-MB-231 cells accounts for *in-situ* generation of $^1O_2$ for inducing PDT, along with the disruption of the MT network and G2/M cell cycle arrest to induce chemotherapeutic effect. Importantly, the Hill plot supports a cooperative effect for **Ru-NAP** as a PDT agent. Control studies confirm that **Ru-NAP** is benign to normal healthy human embryo kidney (HEK293) cells under dark and light irradiation compared to MDA-MB-231 cells. The higher efficacy of **Ru-NAP** towards live MDA-MB-231 cells is also reflected in the significantly higher inhibition of tumour growth in the MDA-MB-231 tumour xthe enograft model with insignificant *in vivo* toxicity. This report demonstrates the proof of concept of MT-targeted and a serum-stable (due to small size and the N-stapled termini of the **NAP** peptide) PS as an effective bimodal (chemotherapeutic and PDT) agent for inhibiting tumour growth. Such examples are rather scarce in contemporary literature.[9, 43-48]

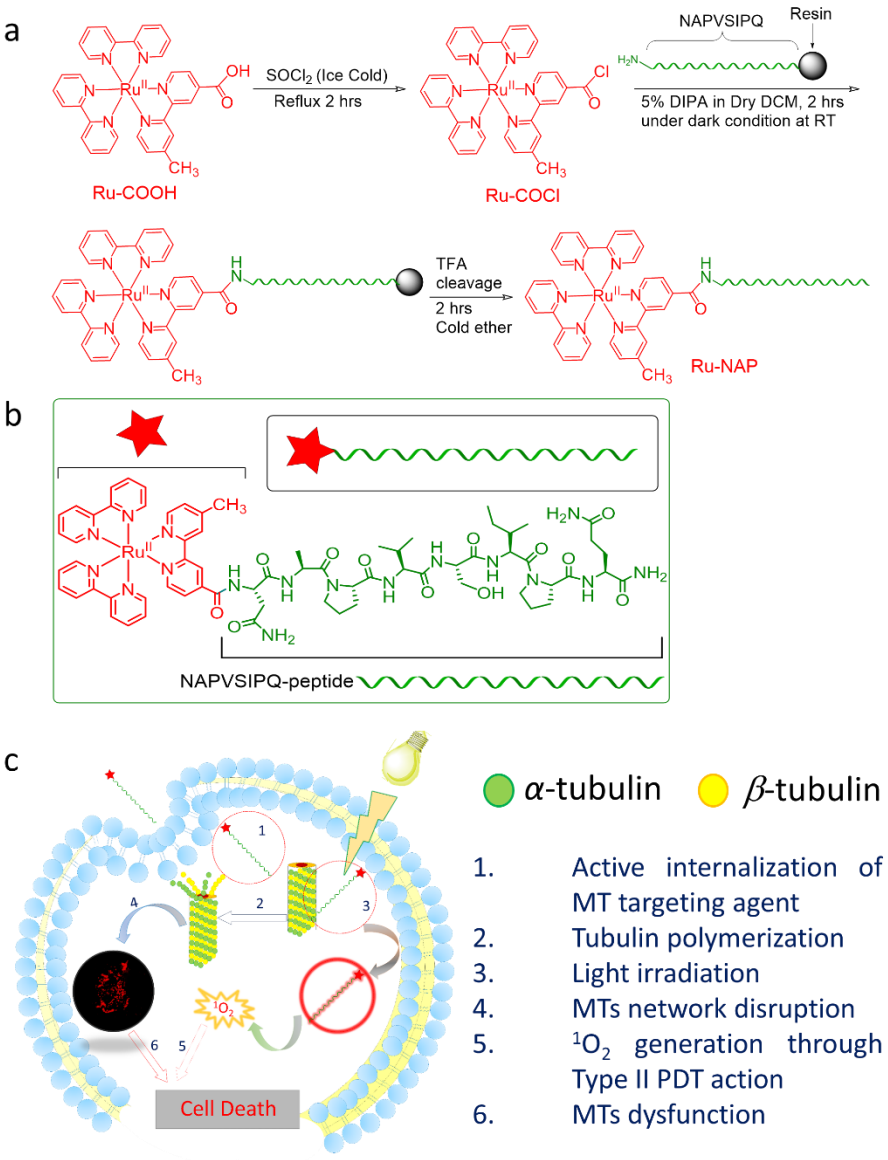

Scheme 1. (a) Cartoon representation of the synthetic methodology adopted for synthesis of **Ru-NAP** and (b) molecular structure of **Ru-NAP**. (c) Schematic representation of microtubule targeted chemotherapeutic and PDT action induced by **Ru-NAP**.

Results and Discussions

Design Strategy of Ru-NAP. Literature reports suggest that the lifetime ($T_{1/2}$) of $^1O_2$ in cytoplasm is about 1×10^{-7} s with a maximum radius of reactive action of 30 nm.[40] While, at low bacterial concentrations during photodynamic inactivation of bacteria, $T_{1/2}$ for $^1O_2$ is reported to be 6 ± 2 μs with a diffusion length of < 50 nm.[49] However, the efficient therapeutic performance of the Type II pathway is hindered by an insufficient supply of molecular oxygen (O_2) in the tumour microenvironment (TME) because of hypoxic tumour cells. Microtubules (MTs) are also involved in manipulation of tumour hypoxia. Hypoxia-inducible factor 1 (HIF-

1), being overexpressed in the TME regulates several target genes involved in tumour angiogenesis, matrix metabolism, apoptosis and glycolysis leading tumor hypoxia.[50] Tumor angiogenesis is triggered by hypoxia via activation of HIF-1 pathway and HIF-1 utilizes microtubules as tracks for their nuclear translocation and transcription followed by hypoxic induction. Thus, targeting and disruption of MTs dynamics serve as potent barriers for tumour angiogenesis through the downregulation of HIF-1 pathway, which is supposed to increase the efficacy of the Type II PDT agents. This motivated us to utilize the **Rubpy** derivative as a MT targeted Type II PDT agent in hypoxic tumour microenvironment.[43, 51-54] **Rubpy** derivatives are an attractive choice as a PS primarily for the high quantum yield for a relatively long-lived transient triplet state (~ 100 ns) that is crucial for $^1O_2$ generation, photochemical stability, amphiphilicity, stability towards photobleaching, insignificant dark toxicity/mutagenicity and facile cellular internalization.[55-56] Importantly, COO^--terminal tails of several acidic amino acid residues of α- and β-tubulins are located on the outer surface of MTs, and this accounts for an overall negatively charged surface. These carboxy-terminal tails, mostly of glutamate side chain on α- and β-tubulins of MTs, are the key sites of interactions for many MT-binding proteins or peptides.[57] The estimated electric field of a single MT is 52.2 electronic charges (e) per dimer.[58-59] These would further favour interaction between the cationic **Rubpy** part of **Ru-NAP**, apart from the binding of **NAP** to the MTs.

Synthesis and Characterization of Ru-NAP and the Control Molecules. With these rationales, **NAP** and **Ru-NAP** were synthesized following procedures that are elaborated in supporting information. **NAP** was synthesized following the standard Hydoxybenzotriazole (HBTU) coupling protocol of the solid phase peptide synthesis (SPPS) method (Scheme S1).[60] The crude peptide was purified using reverse phase high performance liquid chromatography (HPLC) with C18 column and acetonitrile-water gradient and purified **NAP** was characterized using HPLC, ^{1}H NMR and ESI-Ms (Figure S1-S3). **Ru-NAP** was also synthesized using SPPS. Firstly, Ru(II)-polypyridyl complex having a pendent carboxy functionality (**Ru-COOH)** was synthesized following a literature report with necessary modification in the purification process (Scheme S2).[61-64] Cis-dichlorobis(bipyridine)ruthenium (II) (**Ru(2,2´-bipy)$_2$Cl$_2$**) and 4´-methyl-2,2´-bipyridine-4-carboxylic acid were dissolved in ethanol-water mixture (1:1) with addition of equivalent amount of Na_2CO_3. The solution was allowed to reflux at 100 ^{o}C for 8 h followed by the addition of saturated aq. solution of KPF_6 to precipitate the crude complex of **Ru-COOH**. The precipitate was purified by column chromatography and characterized using ^{1}H NMR and ESI-Ms (Figure S4-S7). Then **Ru-COOH** was converted to acid-chloride

intermediate (**Ru-COCl**) and conjugated to **NAP** peptide bound Rink amide resin by SPPS method.[61] This resin-attached **Ru-NAP** was further subjected to TFA cleavage and cold ether treatment to yield crude **Ru-NAP**. The crude **Ru-NAP** was purified using reverse phase HPLC (C18 column and acetonitrile-water gradient) and characterized using HPLC, ^{1}H NMR and ESI-Ms (Scheme 1, S2 and Figure S8-S10). Pyrene is known to increase the hydrophobicity and self-assembled efficacy of the **NAP**. We also synthesized a pyrene-conjugated NAP peptide derivative (**Py-NAP**, Scheme S3) for our control studies using the SPPS method. Detailed synthetic procedures and characterization data required to ensure the desired purity of **Py-NAP** are provided in the supporting information. After synthesis, **Py-NAP** was purified using reverse phase HPLC (C18 column and acetonitrile-water gradient) and characterized using HPLC, ESI-Ms (Figure S11, S12). We further synthesized 4-nitro-2,1, 3-benzoxadiazole (NBD) conjugated NAP (**NBD-NAP;** Scheme S4, S5) for checking the aggregation inside the cell and characterized using HPLC, ^{1}H NMR and ESI-Ms (Figure S13-S16).

Photophysical Studies of Ru-NAP. After successful synthesis, we performed the photo-physical studies of the **Ru-NAP** and were compared it with the commercially available PDT agent **Rubpy**. The electronic and fluorescence spectrum of **Rubpy** and **Ru-NAP** were recorded. A distinct red shift in the respective absorption (461 nm, $\Delta\lambda_{Abs}$ = 7 nm) and emission (651 nm, $\Delta\lambda_{Ems}$ = 37 nm) maximum was observed for **Ru-NAP** as compared to **Rubpy** in PBS buffer (pH 7.4; Figure S17). The relative emission quantum yield ($\Phi_{Em}^{Ru\text{-}NAP}$) for **Ru-NAP** was evaluated as 0.70 (**Rubpy** as reference) in deionized water, saturated with O_2 (Figure S18). Considering the substitution of one 2,2´-bipy with **NAP** functionalized 2,2´-bipy through an amide linkage in **Ru-NAP**, these red shifts are anticipated. Luminescence lifetimes of the **Ru-NAP** (291.7 ± 1.002 ns) and **Rubpy** (366 ± 1.42 ns) using λ_{Ex} = 450 nm; $\lambda_{Em}^{Ru\text{-}NAP}$ = 651 nm and λ_{Em}^{Rubpy} = 614 nm in aq. PBS buffer (pH =7.4) at room temperature (RT) were evaluated (Figure S19 and Table S1). Typically, such molecules with an extended luminescence lifetime are better suited for use as a PDT agent.[27, 65-68]

Docking and Simulations Studies. We performed docking studies to check the validity of our design rationale and also to understand the possible binding site for **Ru-NAP** to tubulin dimer. Both **NAP** and **Ru-NAP** showed thermodynamically favourable binding interaction with the tubulin as reflected in the negative binding free energies (Table S2-S4). The average binding energy values obtained for **NAP** and **Ru-NAP** are -6.77±0.61 and -8.28±0.87 kcal/mol, respectively. A paired t-test showed significantly lower binding energy for **Ru-NAP** than **NAP**

(p-value: 0.000091). The dissociation constant (K_D) obtained for **Ru-NAP** is one order of magnitude lower than **NAP** suggesting higher affinity (K_a) binding for **Ru-NAP**. The respective binding constant of **NAP** and **Ru-NAP** is found to be 9.24 x 10^4 M^{-1} and 1.19 x 10^6 M^{-1} showing higher binding of **Ru-NAP** compared to **NAP** (Table S5). Blind docking of **NAP** and **Ru-NAP** on the tubulin dimers showed potential binding sites including the taxol binding sites as depicted in Figure S20. Further targeted docking to the taxol binding site on β-tubulin produced low-energy binding modes (Table S4 and Figure S21). Computational studies suggest two low-energy binding modes of **Ru-NAP**: Ru-head is bound to the taxol binding site (**Ru-NAP complex 1**) and the peptide tail is bound to the taxol binding site (**Ru-NAP** complex 2). Previous literature also suggests the binding of the NAP-peptide to the taxol binding site.[69] MD simulations showed very stable binding of the **NAP** as well as **Ru-NAP** with tubulin throughout the simulation time (Figure S22). Figure 1a-1e shows the snapshot of MD simulation for the **Ru-NAP** and tubulin complexes in two possible binding conformations. RMSD profiles of the MD simulations, interacting residues with interaction fractions and the schematics of the interactions are shown in Figures S23-S31. Water plays an important role in the binding interaction of the peptide as evident from the several water bridges formed during the MD simulation (Figure S26-S31). It was also observed that the bipyridyl moieties of the **Ru-NAP** head group may interact with the tyrosine side chains by forming pi-stacking interactions (Figure 1a-1e and S31). The role of cationic Ru(II)-polypyridyl moiety is important in the binding of **Ru-NAP** with tubulin as tubulin remains highly negatively charged at neutral pH. Charges on tubulin alpha and beta chains are -12 each, therefore, the contribution of long-range electrostatic interaction with the cationic Ru(II)-core of Ru(II)-polypyridyl moiety significantly drives this bimolecular association (Table S6 and S7).

Binding of Ru-NAP with tubulin. The binding of **NAP** or **Ru-NAP** to tubulin was evaluated following a conventional luminescence quenching process of tryptophan (Trp) of tubulin as a function of [**NAP**] or [**Ru-NAP**].[70-73] Decrease in intrinsic tryptophan fluorescence of tubulin upon binding of **NAP** or **Ru-NAP** with tubulin indicates that its' binding causes perturbation of tubulin conformation in the vicinity of Tryptophan residues (Figure 1f and 1g). The linearity of the Stern-Volmer plot confirms dynamic quenching process, while the experimental data show a much higher binding between **Ru-NAP** and tubulin ($K_a^{\text{Ru-NAP-tubulin}}$ = (6.8 ± 0.55) x 10^6 M^{-1}), as compared to **NAP** and tubulin ($K_a^{\text{NAP-tubulin}}$ = (8.2 ± 1.1) x 10^4 M^{-1}). This also agrees well with the results of the docking studies. This further corroborates our proposition that the

cationic Ru(II)-polypyridyl moiety in **Ru-NAP** favours a stronger binding to β-tubulin than **NAP**.

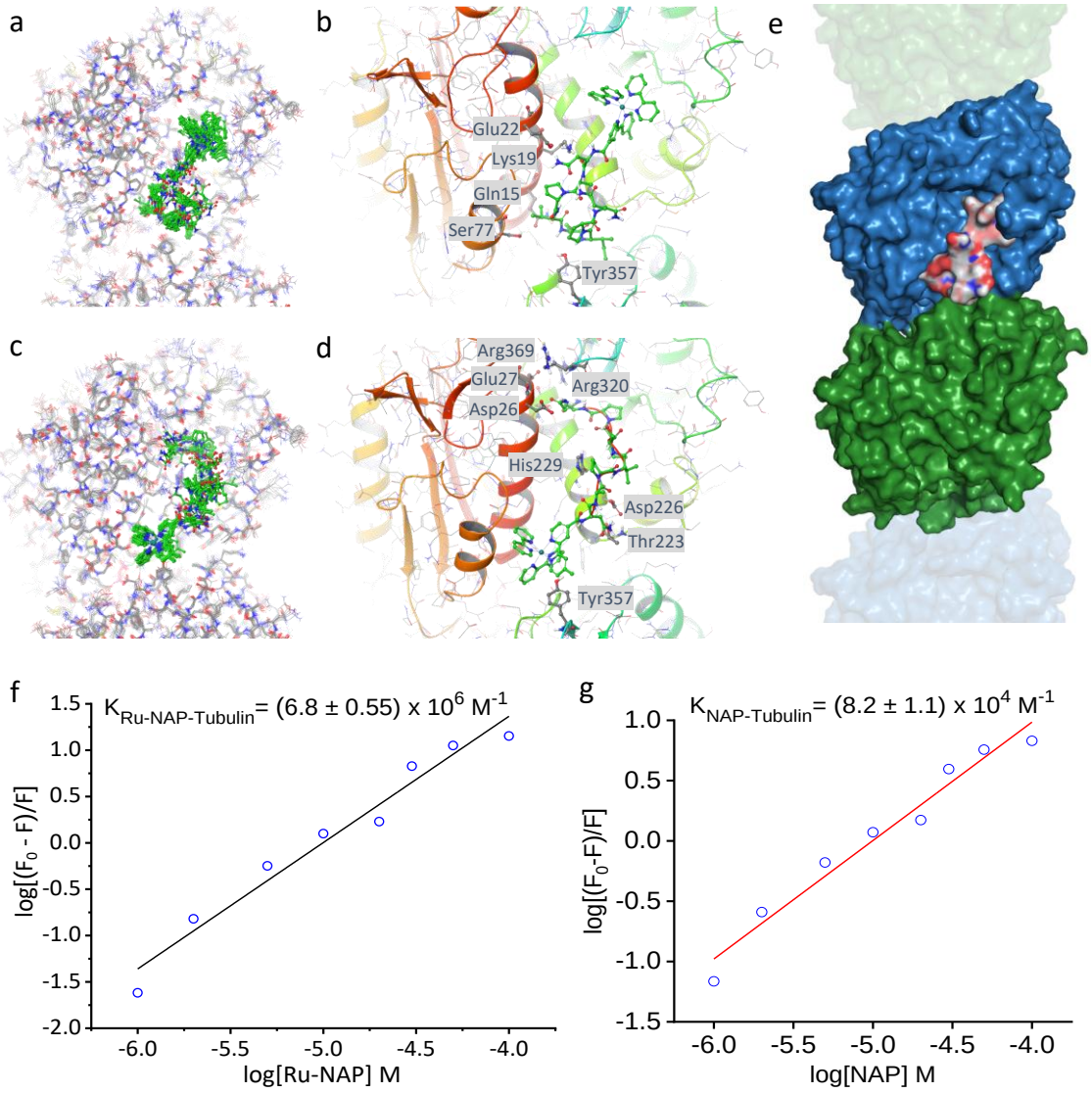

Figure 1. Binding interaction of Ru-NAP with tubulin. (a) Tubulin-**Ru-NAP** complex **1**. Snapshots from the MD simulation are superimposed. **Ru-NAP** is shown in green. (b) A close-up view of the last frame of the MD trajectory with interacting residues is highlighted. (c) Tubulin-**Ru-NAP** complex **2**. (d) Interacting residues. (e) The surface representation shows binding of **Ru-NAP** (pink) on β-tubulin (blue). The α-subunit is shown in green. Binding constant curve of (f) tubulin and **Ru-NAP** and (g) tubulin and **NAP** from the study of quenching of Tryptophan fluorescence of tubulin in the presence of different concentrations (1-100 μM) of **Ru-NAP** or **NAP** in BRB80 buffer ((80 mM PIPES, 1 mM EGTA, 1 mM $MgCl_2$, pH 6.9) at 25 °C.

Ru-NAP Forms Fibrillar Aggregates. NAP peptide is known to form fibrillar structures when incubated for 7 days.[74-75] We studied the morphology of **NAP**, **Py-NAP** and **Ru-NAP** after incubation for 5 days in aq. 1X PBS buffer using transmission electron microscopy (TEM). **NAP** forms the fibrillar structure as previously reported (Figure 2a, 2b). TEM images recorded for **Py-NAP** also showed fiber-like morphology (Figure 2c). Better fiber formation for **Py-NAP**, compared to **NAP** under identical conditions could be ascribed to the ability of Py moiety to participate in cation-π/π-π stacking interactions. Importantly, the degree of the fiber formation was more extensive for **Ru-NAP**, as compared to **NAP** or **Py-NAP** (Figure 2d). Literature reports suggest that cationic $Fe^{II}(2,2´\text{-bipy})_3^{2+}$ moiety in $Fe^{II}(2,2´\text{-bipy})_3^{2+}$-collagen conjugate favours the self-assembly process and the fiber formation.[76] A similar phenomenon was observed in the present study. Importantly, the extent of fiber formation for **Py-NAP** was lower than that of **Ru-NAP**, when both were subjected to self-assembly to form fiber under identical conditions. This presumably arises from a head-to-tail orientation of the **Ru-NAP** molecules during the self-assembly process for the fiber formation (Figure 2a). The self-assembly behaviour of **NAP**, **Py-NAP** and **Ru-NAP** was further confirmed using scanning electron microscopy (SEM). The SEM images for **NAP** show short fiber formation (Figure 2e), which is found to be improved in the case of **Py-NAP** and **Ru-NAP** (Figure 2f and 2g). Figure S32 show the histogram of the average diameter of the **NAP**, **Py-NAP** and **Ru-NAP** fibers. These indicate that **Rubpy** favoured the self-assembly process in **Ru-NAP**.

Dark Stability and Photo Stability of Ru-NAP. We investigated the dark and photo stability of the **Ru-NAP** and compared these with **Rubpy**. Both complexes showed insignificant degradation in the dark when incubated in 1X PBS buffer (pH 7.4) for 12 h (Figure 2h and S33). The stability of **Rubpy** and **Ru-NAP** after successive irradiation with a 450 nm laser (200 $mW.cm^{-2}$, 1 min, 12 $J.cm^{-2}$) in 1X PBS buffer (pH 7.4) was examined (ESI). Only an insignificant bleaching was observed for **Rubpy**, while a slight degradation (<7 %) was observed for **Ru-NAP** due to photobleaching even after 5 cycles (Figure 2i and S33). This ensured that the conjugation of **NAP** to **Rubpy** in **Ru-NAP** had no influence on its dark stability, while a marginal decrease in its photo stability characteristics was observed.

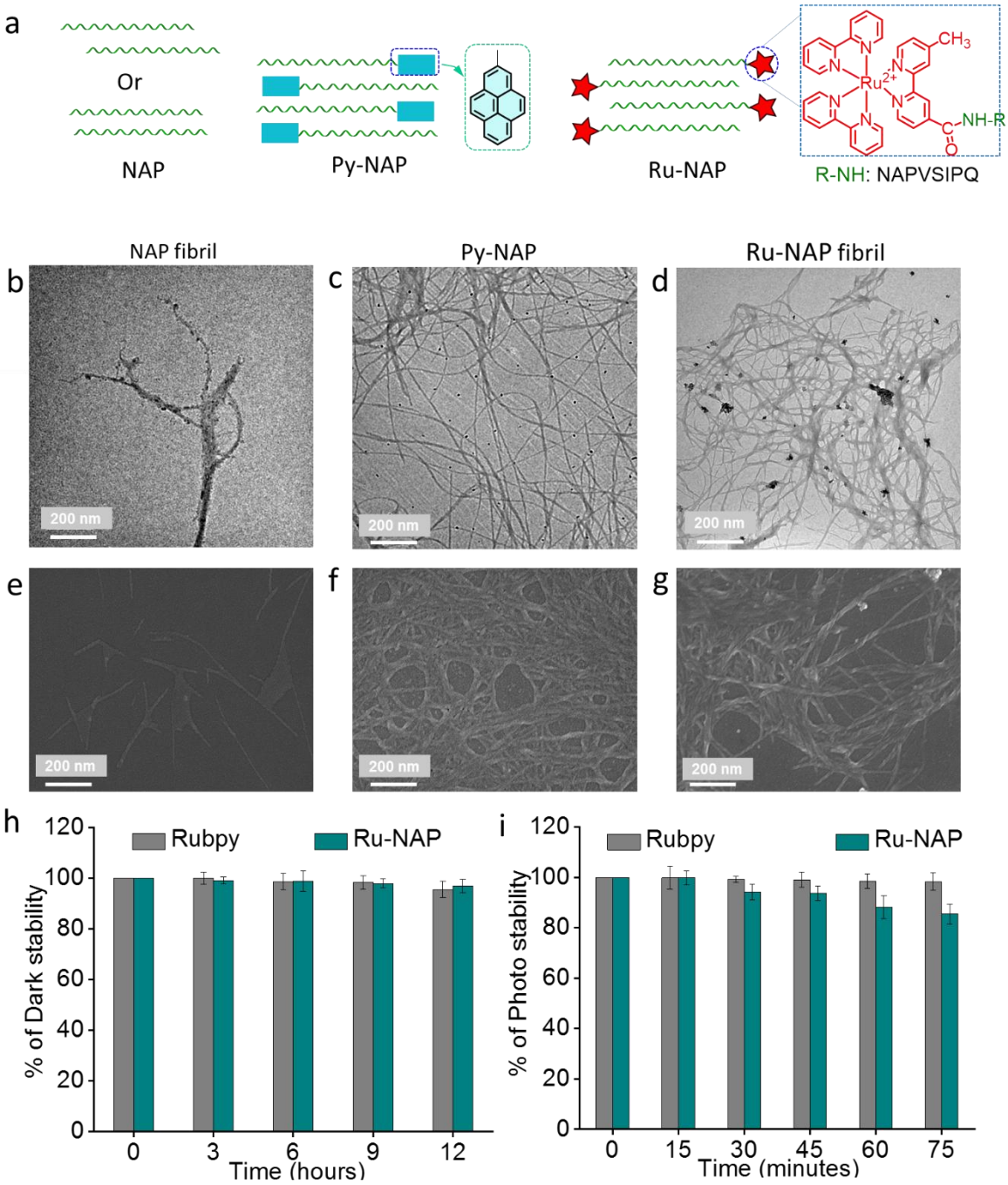

Figure 2. (a) Schematic representation of the self-assembly of **NAP**, **Py-NAP** and **Ru-NAP**. TEM images of (b) **NAP** (100 μM; 1X PBS buffer (pH = 7.4), while (e) represents the corresponding SEM image. (c) TEM image of **Py-NAP** (100 μM; 1X PBS buffer (pH = 7.4) containing 2.5% DMSO (v/v), while (f) represents the corresponding SEM image. (d) TEM image of **Ru-NAP** (100 μM; 1X PBS buffer (pH = 7.4) containing 2.5% DMSO (v/v), while (g) represents the corresponding SEM image. (h) Dark stability of **Rubpy** and **Ru-NAP** using 75 μM of each of these complexes in 1X PBS buffer (pH = 7.4) containing 1% DMSO (v/v).

Absorbances were recorded in 3 h intervals up to 12 h. (i) Photo stability of **Rubpy** and **Ru-NAP** using 75 μM of each of these complexes in 1X PBS buffer (pH = 7.4) containing 1% DMSO (v/v). Absorbance was recorded after irradiation for 1 min with 450 nm laser light (200 $mW.cm^{-2}$; 1 min, 12 $J.cm^{-2}$) in 15 min intervals up to 75 min. The ± SD was calculated from three independent sets of experiments.

Type II ROS Generation of Ru-NAP. To investigate the efficacy of **Ru-NAP** in generating $^1O_2$, we performed 1,3-diphenylisobenzofuran (DPBF) assay in Milli-Q water containing 1% DMSO (v/v). The absorbance of DPBF was found to decrease gradually when DPBF was irradiated for 15 s in the presence of **Ru-NAP** with a 450 nm laser (Figure 3a, S34a and S34b). However, the absorbance of DPBF remained unaltered when identical experiments were performed without any 450 nm irradiation. This confirmed the *in-situ* ROS generation on irradiation of **Ru-NAP** with 450 nm. DPBF assay is used for the detection of $^1O_2$, apart from other ROS species.[77] To reconfirm the in-situ generation of $^1O_2$ as a transient species, we further performed an additional 9,10-anthracenediyl-bis(methylene)dimalonic acid (ABDA) assay, which is specific for $^1O_2$.[78] A successive decrease in the absorbance of ABDA was observed after irradiation with 450 nm light in the presence of **Ru-NAP** in Milli-Q water. The reaction of ABDA with $^1O_2$, generated *in situ*, on irradiation of **Ru-NAP**, accounted for this observed gradual decrease in absorbance (Figure 3b, S34c and S34d). However, control experiments revealed that the absorbance of ABDA remained unaltered for **Ru-NAP** treated solution without photo irradiation. This further corroborated our presumption that the **Ru-NAP** belonged to the Type II PDT agent. The DPBF and ABDA assays for **Rubpy** also confirm $^1O_2$ generation but to a lesser extent than the **Ru-NAP** (Figure S35). The quantum yield for $^1O_2$ generation (Δ^1O_2) for **Ru-NAP** was evaluated as 0.55 by UV-Vis titration studies of DPBF using Methylene Blue (MB) as a reference (Figure S36). This is a reasonably high value because we used Milli-Q water medium saturated with O_2 and is higher than the desired value ($\Delta^1O_2 = 0.5$) for any PDT applications.[79] These data confirmed the therapeutic potential of Ru-NAP on irradiation upon 450 nm light. Next, the possibility of the generation of Type I ROS (hydroxyl radical ($^{\bullet}OH$) or/and superoxide radical ($O_2^{\bullet-}$) as a transient species on irradiation of **Ru-NAP** with 450 nm light was examined. Typical Terephthalic acid (TPA) and 5,5´-dimethyl-1-pyrroline N-oxide (DMPO) based assays were performed respectively to identify the formation of transient ROS species like $^{\bullet}OH$ and $O_2^{\bullet-}$ on irradiation of **Ru-NAP** with 450 nm light (Figure S37, ESI). These results confirm that **Ru-NAP** failed to induce the formation of Type I PDT under the experimental conditions.[80-81]

Lipophilicity Measurement of Ru-NAP. Appropriate lipophilic balance, rather than the overall charge of the compound, is an important parameter for effective cellular internalization. Lipophilicity takes care of the solvation ability of molecules in fats and lipids, as well as in aqueous media. It can be correlated with cellular internalization and uptake.[82-84] The distribution coefficient (log P) of **NAP**, **Rubpy** and **Ru-NAP** were evaluated in an octanol-water mixture using shake-flask method. The evaluated lipophilicity of the **Ru-NAP** was higher than that of **Rubpy** (Figure 3c and S38). Higher lipophilicity improves the cellular internalization process and helps to overcome accumulation defects with consequential cytotoxicity.[85-86]

Effect of Ru-NAP on Tubulin Dynamics, Buffer and Serum Stability of Ru-NAP. A literature report suggests that **NAP** interacts with MT end-binding proteins (EB1 and EB3) and increases the dendritic spine density.[87] We examined the binding of the **Ru-NAP** to the tubulin and its' influence on the tubulin polymerization process using a fluorescence-based tubulin polymerization assay (BK006P). The extent of the light scattered by MT is proportional to the concentration of microtubule polymer. A plot of the extent of light scattered as a function of the time yielded the polymerization curve depicting the nucleation, growth, and steady-state equilibrium (Figure 3d). It is evident from Figure 3d that **Ru-NAP** is more efficient in stabilizing the microtubule and enhances tubulin polymerization in comparison to **NAP** (used in equimolar concentration), used as a positive control. Next, we checked the stability of the **Ru-NAP** in 1X PBS buffer (pH = 7.4) and fetal bovine serum (FBS, 20% v/v in 1X PBS buffer (pH = 7.4)) up to 24 h. The HPLC analysis of the Ru-NAP (100 μM) incubated sample in both PBS and 20% FBS showed > 95% and > 80% stability respectively till 24 h due to small size and the N-stapled termini of the **NAP** peptide (Figure 3e, 3f and S39).

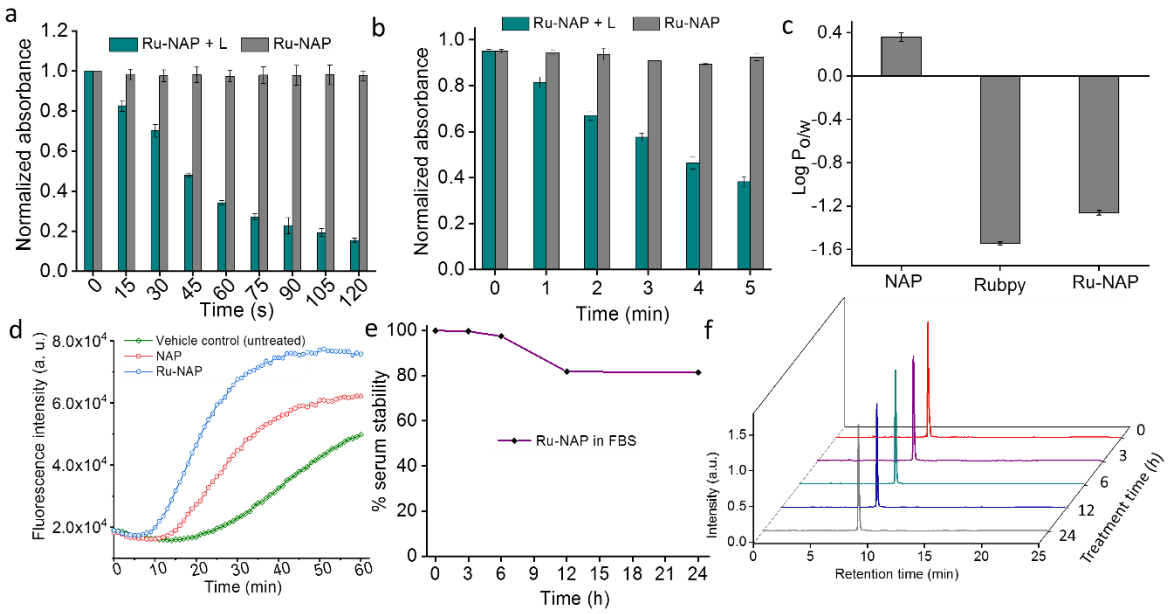

Figure 3. (a) Changes in absorbance of DPBF treated with **Ru-NAP** ([DPBF] = 125 μM and **[Ru-NAP]** = 2.5 μM in Milli-Q water containing 1% DMSO (v/v)) were recorded at 419 nm following irradiation with 450 nm light (200 $mW.cm^{-2}$, 15 s, 3 $J.cm^{-2}$). (b) Changes in absorbance of [ABDA] (80 μM) treated with **[Ru-NAP]** (1.6 μM) in Milli-Q water under irradiation of 450 nm light (200 $mW.cm^{-2}$, 1 min, 12 $J.cm^{-2}$). (c) Determination of lipophilicity of **NAP, Rubpy** and **Ru-NAP** by shake-flask method using an equal mixture of octanol-water mixture. The lipophilicity of the **Ru-NAP** was found to be increased compared to the **Rubpy**. (d) Fluorescence-based tubulin polymerization assay of **NAP** and **Ru-NAP** using the fluorescence-based tubulin polymerization assay (Cat. # BK011P) from Cytoskeleton. (e) Stability of **Ru-NAP** (%) and (f) time-dependent HPLC of **Ru-NAP** in fetal bovine serum (FBS, 20% v/v in 1X PBS buffer (pH = 7.4)) up to 24 h. The HPLC analysis of the **Ru-NAP** (100 μM) incubated sample in 20% FBS showed >80% stability up to 24 h.

Cellular Uptake of Ru-NAP. NAP is known to be a cell-penetrating peptide. As discussed earlier, presumably, the endocytosis pathway rather than membrane translocation prevailed at the low concentration used for our studies at physiological conditions.[88] We checked the morphology of **Ru-NAP** in RPMI medium supplemented with 10% fetal bovine serum used for the cell culture. The TEM and SEM images of **Ru-NAP** also shows the fiber formation (Figure S40). Next, we investigated the effective cellular uptake of **Ru-NAP** using high-resolution live cell confocal laser scanning fluorescence microscopy (CLSFM) imaging in MDA-MB-231 cell. MDA-MB-231 cell line is ER, PR, and E-cadherin negative and expresses mutated p53. These cells also lack the growth factor receptor HER2 and represent a good model of triple-negative breast cancer.[89] Four hours post-treatment was found to be adequate for

internalization of **Ru-NAP** (5 μM) into the cellular cytoplasm (Figure 4a; see merged image with bright field). We further checked the cellular uptake of the **Ru-NAP** in MDA-MB-231 and HEK293 cells using Inductive Coupled Plasma-Mass Spectroscopy (ICP-MS). The result shows a ~2.6-fold higher accumulation of **Ru-NAP** in live MDA-MB-231 cells compared to that of live HEK293 cells (Figure S41). We have performed new live cell CLSFM by incubating live MDA-MB-231 cells with **Ru-NAP** at 37 °C and 4 °C to examine active or passive uptake of the drug. Interestingly, we observed a 90% reduction in **Ru-NAP** Mean Fluorescence Intensity (MFI) inside cells at 4 °C compared to 37 °C suggesting an energy-dependent uptake of **Ru-NAP** in live MDA-MB-231 cells through endocytosis process (Figure 4b and S42). This indicates the active cellular internalization of **Ru-NAP**. To further confirm the role of endocytosis for the **Ru-NAP** uptake inside cells, we have applied a range of endocytosis inhibitors namely, sucrose (Clathrin endocytic inhibitor), Methyl-β-Cyclodextrin (M-β-CD; caveolin endocytic inhibitor) and amiloride (macropinocytosis inhibitor). CLSFM data indicate a significant reduction in **Ru-NAP** uptake ($p < 0.001$) in cells following pretreatment with sucrose (Figure 4c and S42). MDA-MB-231 cells pretreated with M-β-CD (caveolin endocytic inhibitor) also show a 5-fold reduction in cellular uptake of **Ru-NAP**. However, pre-treatment with amiloride showed insignificant changes in **Ru-NAP** cellular uptake under similar conditions. These results indicate clathrin and caveolin-dependent endocytic processes are involved in the uptake of **Ru-NAP** in MDA-MB-231 cells. To ascertain the molecular aggregate inside the live MDA-MB-231 cells, we further used fluorescence imaging studies using **NBD-NAP**. Being an environmentally sensitive fluorophore, NBD is frequently used to ascertain the formation of molecular assembly(ies) in the cellular milieu. NBD derivatives typically show strong fluorescence as they get readily partitioned into hydrophobic pockets and this is accompanied by a characteristic green NBD fluorescence maximum (λ_{Em} = 540 nm) following excitation at 470 nm.[90] Internalization of **NBD-NAP** with subsequent partitioning within the fibrillar aggregates in live MDA-MB-231 showed a strong green fluorescence to confirm significant fiber of **NBD-NAP** (Figure S43). However, such fiber is less prominent in HEK293 cells due to less cellular uptake compared to MDA-MB-231 cells (Figure S44). This supports our presumption on intracellular fibers of analogous molecule of **Ru-NAP**.

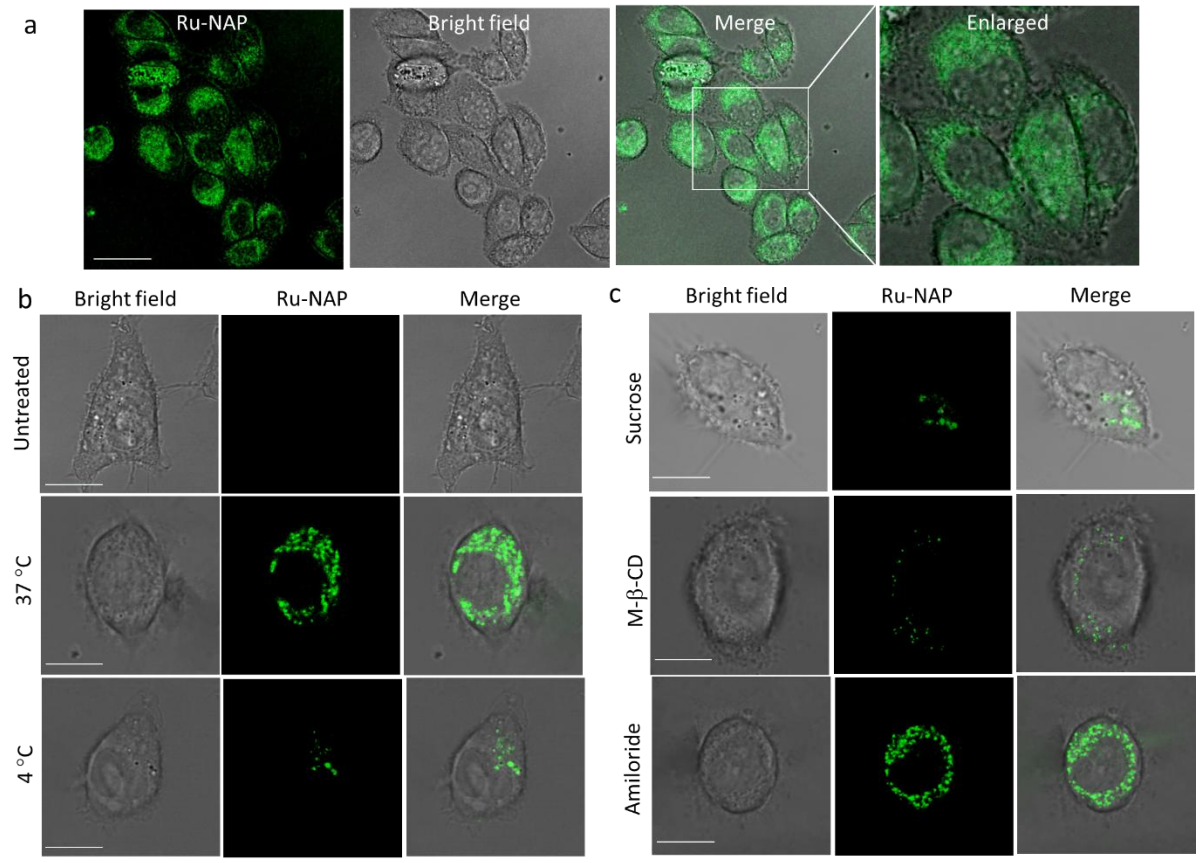

Figure 4. Representative CLSFM images showing accumulation of **Ru-NAP** (**Ru-NAP** shows intrinsic green fluorescence) in live MDA-MB-231 cells (a) incubated with **Ru-NAP** (5 µM for 4 h; Scale bar, 5 µm) at 37 °C, (b) untreated (upper row) and incubated with 5 µM **Ru-NAP** for 4 h at 37 °C (middle row) or 4 °C (bottom row) and (c) pre-incubated with 400 mM sucrose for 30 min (upper row) or 10 mM M-β-CD for 30 min (middle row) or 3 mM amiloride for 15 min (bottom row).

Co-localization of Ru-NAP with Tubulin/MT. To verify if **Ru-NAP** was localized on the MTs, we incubated MDA-MB-231 cells with **Ru-NAP** (20 µM for 4 h), co-stained them with the microtubule-specific marker tubulin (EP1332Y), and analysed them via CLSFM (Figure 5a). Significant co-localization of **Ru-NAP** with tubulin was detected, suggesting a strong association of **Ru-NAP** with MTs. A detailed plot profile analysis demonstrates significant co-localization of the green-colored **Ru-NAP** and red-colored tubulin (Figure S45). Co-localization analysis of **Ru-NAP** (green) with tubulin (red) showed a Pearson Coefficient (R) of 0.88. This seems rational considering the improved lipophilicity, and higher surface charge affinity for **Ru-NAP** as compared to **NAP**, which is otherwise known to bind preferentially to β-tubulin. These contributed to the higher evaluated binding constants for **Ru-NAP** compared

to **NAP** (control) towards β-tubulin and confirmed the high targeting ability of the **Ru-NAP** to MT in live MDA-MB-231 cells.

Cytotoxicity Study of Ru-NAP. MT serve as 'freeways' for intracellular trafficking. Such fiber formation on the MT surface and/or inside the tubular structure of MT would further interfere with the intracellular trafficking of vesicles and organelles, transport of cargo by motor proteins from the kinesin/dynein superfamilies and ion transport, apart from binding to many MT-binding proteins, which collectively have a serious implication on cellular motility and cell death.[57, 91] So, we assessed the dark toxicity (chemotherapeutic effect) of the **Ru-NAP** in MDA-MB-231 cells for 24 h using MTT assay. **Ru-NAP** shows certain cytotoxicity in the dark and the corresponding IC_{50} value is 2.9 ± 0.5 μM indicating the significant chemotherapeutic effect of the **Ru-NAP** due to the binding of the **Ru-NAP** fibers to the tubulin/MT of the MDA-MB-231 cells (Figure 5b). The dark toxicity of the **Ru-NAP** is much higher than that of **Rubpy** (IC_{50} of **Rubpy** under dark is 21.1 ± 4.2 μM; Figure 5c). Next, we assessed the PDT efficacy of the **Ru-NAP** and compared the same with the **Rubpy** as control. The MDA-MB-231 cells were incubated with varying concentrations of **Ru-NAP** and **Rubpy** for 4 h followed by the light irradiation (450 nm, 200 $mW.cm^{-2}$, 5 min, 60 $J.cm^{-2}$) and further kept in the dark for another 24 h. The cytotoxicity data revealed that **Ru-NAP** showed significant light toxicity to the MDA-MB-231 cells with $^{Light}IC_{50}^{Ru\text{-}NAP}$ value of 32.5 ± 7.8 nM, a value that is ~ 89 times lower than **Ru-NAP** ($^{Dark}IC_{50}^{Ru\text{-}NAP}$ = 2.9 ± 0.5 μM, Figure 5b) due to its' combined effect of chemotherapeutic through the induction of higher MT polymerization and PDT. It is noteworthy that **Rubpy** shows certain cytotoxicity in the dark and upon light irradiation. The IC_{50} of dark toxicity of **Rubpy** [$^{Dark}IC_{50}^{Rubpy}$] is 21.1 ± 4.24 μM and the IC_{50} of light toxicity of **Rubpy** $^{Light}IC_{50}^{Rubpy}$ (0.24 ± 0.05 μM; Figure 5c). Most importantly, $^{Dark}IC_{50}^{Ru\text{-}NAP}$ (2.9 μM) is lower by ~ 7.2 times and $^{Light}IC_{50}^{Ru\text{-}NAP}$ value is lower by ~7.3 times than that for $^{Dark}IC_{50}^{Rubpy}$ (21.1 μM) and $^{Light}IC_{50}^{Rubpy}$ (0.24 μM) respectively. Thus, these data reveal that **Ru-NAP** is more cytotoxic than **Rubpy** due to its' chemotherapeutic effect and **Ru-NAP** on light irradiation shows a substantially low IC_{50} value of 32.5 nM towards live MDA-MB-231 cancer cells (Figure 5b and 5c, Table S8).[56] The **NAP** peptide alone did not show light or dark toxicity towards live MDA-MB-231 cells up to 200 μM concentration and this agreed well with the literature reports (Figure S46).[37] To check the PDT effect of **Ru-NAP** in non-tumourigenic normal human embryo kidney cells (HEK293) cells, these cells were incubated with varying concentrations of **Ru-NAP** for 4 h in the dark. These pre-treated cells were then irradiated for 5 min (450 nm, 200 $mW.cm^{-2}$, 5 min, 60 $J.cm^{-2}$) and kept in the dark for another

24 h. It showed a much lower toxicity towards HEK293 cells ($^{Light}IC_{50}^{Ru\text{-}NAP}$[HEK293] 17.2 ± 2.5 μM; Figures 5e) compared to MDA-MB-231 cells ($^{Light}IC_{50}^{Ru\text{-}NAP}$ value of 32.5 nM). Importantly, **Ru-NAP** under dark incubation for 24 h did not show detectable toxicity up to 80 μM towards HEK293 cells (Figure 5f). However, **Rubpy** shows significant dark and light toxicity to the HEK293 cells (Figure 5e and 5f). The **NAP** peptide alone did not show light or dark toxicity up to 200 μM concentration towards live HEK293 cells (Figure S47). We further checked the photo toxicity of the **Ru-NAP** after irradiation with green light (520 nm) and red light (630 nm), apart from the blue light (450 nm). Irradiation with red light shows insignificant photo toxicity (IC_{50} is similar to that of dark toxicity), while this is most prominent when blue light (450 nm) is used (Figure S48b and Table S8). Irradiation with green light show slightly lower PDT effect compared to the one observed with blue light (Figure S48a and Table S8). Minimal PDT effect of red light compared to the green light and blue light correlate well with the relative difference in the molar absorptivity of **Ru-NAP** in the respective spectral zone. We further performed the dark toxicity and phototoxicity of the **Ru-NAP** under blue light irradiation in human cervical cancer (HeLa) cells and human breast cancer (MCF7) cells. **Ru-NAP** showed similar dark and phototoxicity to that of MDA-MB-231 cells (Figure S49). Table S8 reveals the IC_{50} value of **Ru-NAP** and **Rubpy** in different cancer and normal cells, along with their respective phototoxic index (PI; IC_{50} under dark/ IC_{50} under light irradiation). The observed high toxicity of **Ru-NAP** in MDA-MB-231 cells compared to HEK293 cells presumably lies in the accelerated metabolic rate of MDA-MB-231 cells as a result of the Warburg effect and the tendency of small molecules to accumulate in cells once they have formed aggregates as in case of **Ru-NAP**.[92-94] We utilized live cell high-resolution CLSFM to test the uptake of **Ru-NAP** (5 μM for 4 h) in MDA-MB-231 cells in the ATP-depleted M1 media supplemented with 10 mM sodium azide and 10 mM 2-deoxy-D-Glucose (inhibitor of glycolysis), allowing us to investigate the Warburg effect. The Mean Fluorescence Intensity (MFI) of **Ru-NAP** decreased ~5 fold in the presence 2-deoxy-D-Glucose which indicates 5-fold reduction in the drug uptake into cancer cells in the presence of glycolysis inhibitors and provides direct evidence for the operation of Warburg phenomenon dependent **Ru-NAP** cellular uptake (Figure S50). Thus, the above results reveal that the conjugation of **NAP** to a **Rubpy** has a profound effect in reducing the IC_{50} of MDA-MB-231 cells compared to two individual candidates (**NAP** and **Rubpy**). These indicate the potentiality of **Ru-NAP** as a bimodal PDT agent compared to **Rubpy** due to the microtubule targeting ability, fiber formation and PDT effect. It is worth mentioning here the IC_{50}^{Light} of various derivatives (with small organic molecules) of Ru(II)-polypyridyl complexes towards various live cancer cells

are typically > 5 μM and considering these, the observed IC_{50}^{Light} (32.5 nM) of **Ru-NAP** is significant.[28, 56, 95] The cell viability vs log[**Ru-NAP**] under light irradiation plot, a dose-response plot, is sigmoidal (Figure 5b) in nature. It has been established that the sigmoidal plots are better than linear ones for explaining the dose-dependent drug efficacy[96] as this demonstrates the *β*-tubulin-specific **Ru-NAP** induces a cooperative influence as obtained from the Hill plot (n= 1.14) in terms of cellular killing by $^1O_2$ and chemo toxic effect of **Ru-NAP** fibers (Figure 5d). n> 1 in the Hill plot indicates the cooperative influence. Next, we performed the dark and phototoxicity of **Ru-NAP** under hypoxia (1% O_2) to confirm the role of MT targeting for the management of the tumor hypoxia. It shows the similar toxicity as in the normoxia (21% O_2), which indicates that the MT targeting is beneficial for **Ru-NAP** as a potential Type II PDT agent (Figure S51). Table S8 indicates the corresponding IC_{50} and the PI of **Ru-NAP** in hypoxia and normoxia.

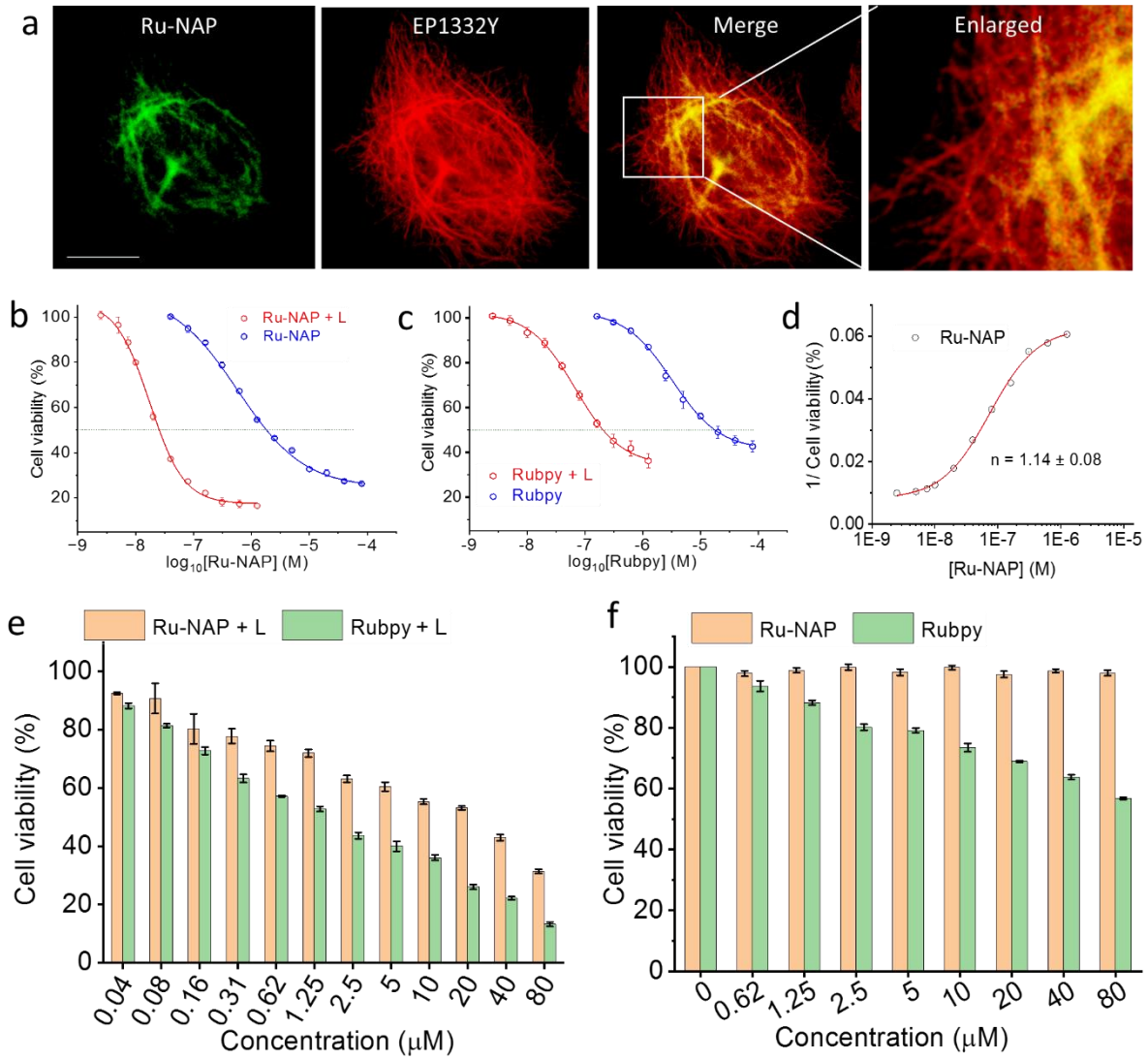

Figure 5. (a) Representative CLSFM images showing co-localization of **Ru-NAP** (20 μM for 4 h; intrinsic green fluorescence) with MT (red fluorescence). Co-localization is shown in the merged image. Merged image indicates the nice co-localization of **Ru-NAP** with the MT (Pearson's coefficient: 0.88). Dose-response profiles of (b) **Ru-NAP** under dark and after light irradiation (450 nm, 200 mW.cm^{-2}, 5 min, 60 J.cm^{-2}) and (c) **Rubpy** under dark and after light irradiation (450 nm, 200 mW.cm^{-2}, 5 min, 60 J.cm^{-2}) from the toxicity data using MTT assay. (d) The Hill plot of the toxicity data of the **Ru-NAP** followed light treatment. (e) Cell cytotoxicity of the **Ru-NAP** and **Rubpy** was measured using MTT assay after light irradiation (450 nm, 200 mW.cm^{-2}, 5 min, 60 J.cm^{-2}) in HEK293 cells. (f) The Dark toxicity of **Ru-NAP** and **Rubpy** in HEK293 cells.

Immunocytochemistry for Investigation the Effect of Ru-NAP on MT/tubulin Network. The high targeting ability to the MTs and significant PDT efficacy of **Ru-NAP** motivated us to examine the mechanistic pathway for cell death. MTs are comprised of α and β-tubulin heterodimers that undergo dynamic cycles of polymerization and depolymerization processes.

A dynamic balance ensures proper cellular functions and survival.[12] To test the dynamics of the MT network following the treatment with **Ru-NAP** and then photoactivation, we performed immunocytochemistry with anti-tubulin antibody in live MDA-MB-231 cells exposed to **Ru-NAP**. Without photoactivation, **Ru-NAP** treatment (20 μM for 4 h) had significant impact on the MT network, indicating perturbation in structural integrity due to the binding of the **Ru-NAP** fibers to MT, accounts for its' chemotherapeutic effect under dark (Figure 6a). Moreover, analogous experiments with light activation showed more significant dose-dependent disruption of the MT network, suggesting an imbalance in the polymerization-depolymerization cycle. This agreed well with the fluorescence-based tubulin polymerization assay showing enhanced tubulin polymerization in the presence of **Ru-NAP**. As a part of the detailed mechanism studies, we checked the effect of **Ru-NAP** on the Actin network of the MDA-MB-231 cells. There is no change in the Actin network of the live MDA-MB-231 cells treated with 20 μM **Ru-NAP** (Figure 6b). Moreover, there is no co-localization of the **Ru-NAP** with actin network indicating the precise targeting of the **Ru-NAP** to the tubulin/MT (Figure 6b). To further validate the tubulin-specific binding/activity of **Ru-NAP**, which promotes specific degradation of the tubulin network in cells, we have performed a tubulin degradation assay following **Ru-NAP** treatment using western blotting. We have tested the expression pattern of the principal cytoskeletal component (Tubulin, Actin with GAPDH) after **Ru-NAP** treatment, coupled with photoactivation. We detected a significant (4-fold) reduction in the tubulin levels compared to the Actin after the cells were treated with **Ru-NAP (**Figure 6c and 6d**)**. Under similar conditions, both Actin and GAPDH levels remained unchanged (See the quantification). These results provide direct evidence for the tubulin-specific binding and degradation by **Ru-NAP** without perturbation of the Actin protein and the cytotoxicity of the **Ru-NAP** is a result of the combined effect of tubulin/MT disruption and huge site-specific $^1O_2$ generation—a distinct demonstration of CALI.

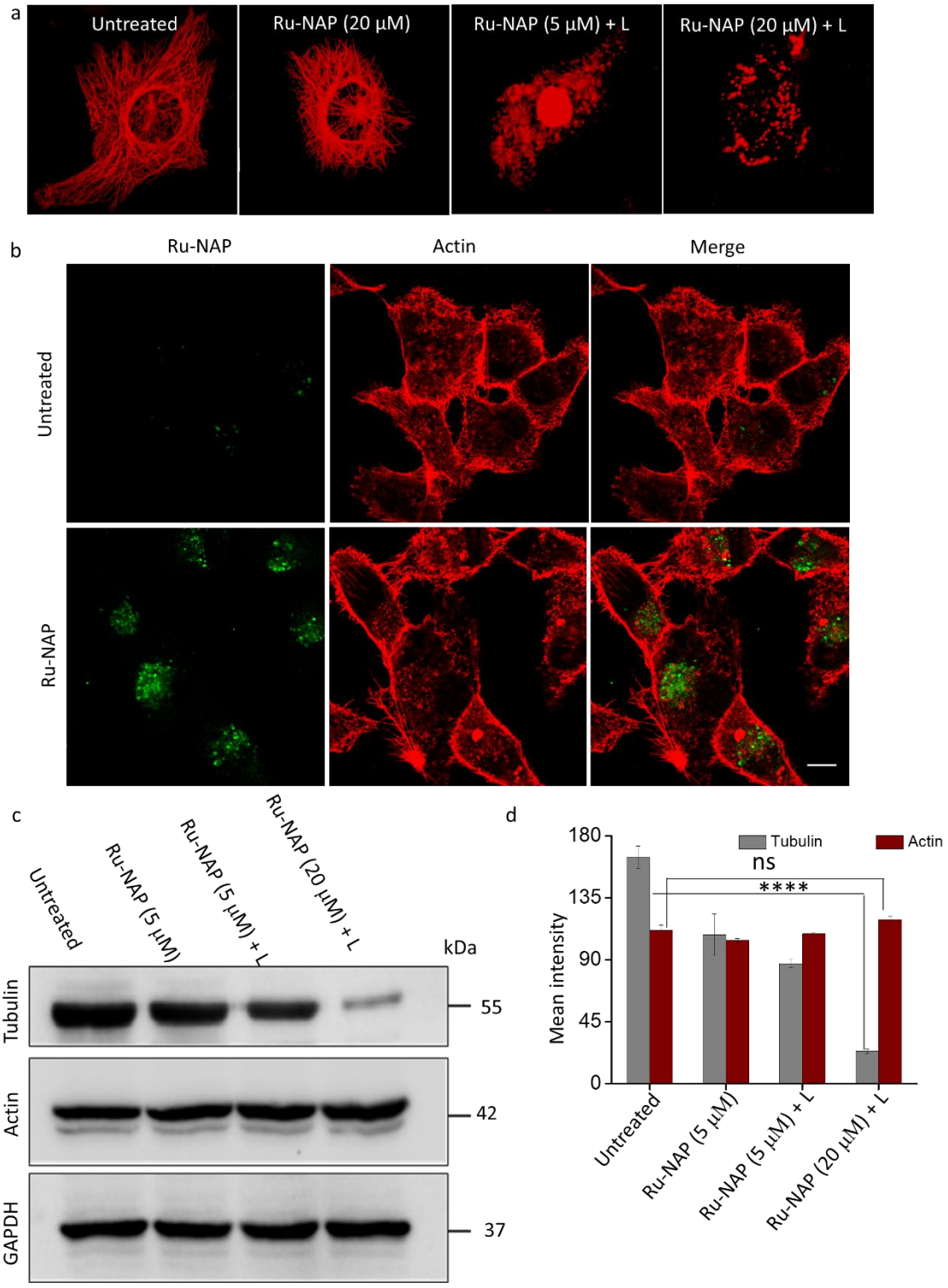

Figure 6. (a) The effect of **Ru-NAP** on the MT/tubulin network in live MDA-MB-231 was studied using CLSFM. A significant disruption of the MT network of the live MDA-MB-231 cells was evident for **Ru-NAP** treatment both under dark and with light irradiation (450 nm, 200 mW.cm^{-2}, 5 min, 60 J.cm^{-2}). (b) The effect of **Ru-NAP** on the Actin network (stained using Alexa Fluor™ 568 Phalloidin) in live MDA-MB-231 was studied in CLSFM. There is no change in the Actin network of the live MDA-MB-231 cells for **Ru-NAP** (20 μM, 4 h)

treatment. (c) Representative Western blots for tubulin, actin, and GAPDH in MDA-MB-231 cells; either untreated or treated with **Ru-NAP** (5 μM or 20 μM) for 4 h with or without blue light photo-activation. GAPDH is shown as the loading control. The migration of protein molecular weight markers is indicated on the right. (d) Densitometry analysis represents the fold change in tubulin, and actin, normalized to GAPDH (error bars represent means ± SEM). Asterisks denote statistically significant differences (***P < 0.001, t test).

Cell Cycle Analysis. We examined the cell cycle of MDA-MB-231 cells using PI/RNase staining following incubation with **Rubpy** or **Ru-NAP** (each of 20 μM for 4 h) and photoactivation followed by the light irradiation (450 nm, 200 $mW.cm^{-2}$, 5 min) and incubation for another 48 h). Treatment with **Rubpy + L** or **Ru-NAP + L** induced a noticeable change in the cell cycle profile (Figure 7a). Results for the **Rubpy + L** treatment at 20 μM revealed a G2/M phase arrest (12.2%) compared to the untreated control (11.3%). In contrast, the use of 20 μM **Ru-NAP + L** showed an enhanced G2/M phase arrest (24.3%). Docking studies revealed that **Ru-NAP** was bound to the β-tubulin part of the MT more efficiently than **NAP** and presumably this had a pronounced influence in stabilizing tubulin polymerization. This was also consistent with co-localization studies and *in vitro* tubulin polymerization experiments, which confirmed that **Ru-NAP** could stimulate MTs polymerization to disrupt MT dynamics. Seemingly, this interferes with the mitotic spindle assembly during metaphase/anaphase transition and triggers the mitotic spindle assembly checkpoint and causes G2/M arrest. Our results are similar to the classical anticancer drugs like Paclitaxel, which induces cell cycle arrest by stabilizing MTs and triggering apoptosis.[97]

Intracellular ROS Generation. Next, we performed flow cytometry-based analysis to quantify ROS produced *in-situ* due to photoirradiation of live MDA-MB-231 cells after treatment with **Rubpy** or **Ru-NAP** or hydrogen peroxide (H_2O_2) as a positive control using CM-H_2DCFDA. We detected significant ROS production upon exposure to H_2O_2 (500 μM, 12 h; Figure S52). Moreover, a significant increase in intracellular ROS for **Ru-NAP + L** (20μM) treated cells was observed compared to Rubpy + L (Figure 7b). These results are consistent with data showing **Ru-NAP** is a Type II PDT inducer that generates $^1O_2$ (*vide infra*) with a relatively high quantum yield of 0.55. These confirmed that the cytotoxicity of the **Ru-NAP** was a combination of ROS-induced cell death and significant disruption of MT dynamics. Taken together, **Ru-NAP** destabilized MTs which triggered cell cycle arrest at the G2/M phase along with ROS-induced cell death, which accounted for the observed cellular cytotoxicity ($^{Light}IC_{50}^{Ru\text{-}NAP}$ 32.5 ± 7.8 nM) in MDA-MB-231 cancer cells.

Flow Cytometry for Analysis of Apoptosis Pathway. The mode of cell death is an important parameter for any chemotherapeutics drugs. We investigated the cell death pathway induced by **Ru-NAP** by flow cytometry using FITC-Annexin V and Propidium Iodide using Doxorubicin (**Dox**) as a positive control for the induction of apoptosis.[98, 99] FITC(-)PI(-) quadrant indicates healthy cells, FITC(+)PI(-) and FITC(+)PI(+) indicates the apoptotic cells and FITC(-)PI(+) indicates the necrotic cells. The cells were treated with **Ru-NAP** (1 µM) for 4 h followed by light irradiation (450 nm, 200 $mW.cm^{-2}$, 5 min, 60 $J.cm^{-2}$) and kept in the dark for another 20 h. The cells were analysed in flow cytometry following incubation with annexin V and PI. A significant fraction (97%) of MDA-MB-231 cells underwent the apoptosis process for **Ru-NAP** treated after light irradiation (Figure 7c). Whereas, 44%, 38%, 47% of cells underwent apoptosis after **Rubpy + L, Ru-NAP** and **Dox** treatment respectively (Figure 7c). Figure 7d shows the histogram of quantitative analysis from the triplicate experiment. This indicated that **Ru-NAP** showed significant apoptosis under dark condition and almost exclusive light-induced apoptosis of the MDA-MB-231 cells through a combination of disruption of the microtubule/tubulin network dynamics and ROS generation and the efficacy of **Ru-NAP** was more pronounced than **Rubpy**.

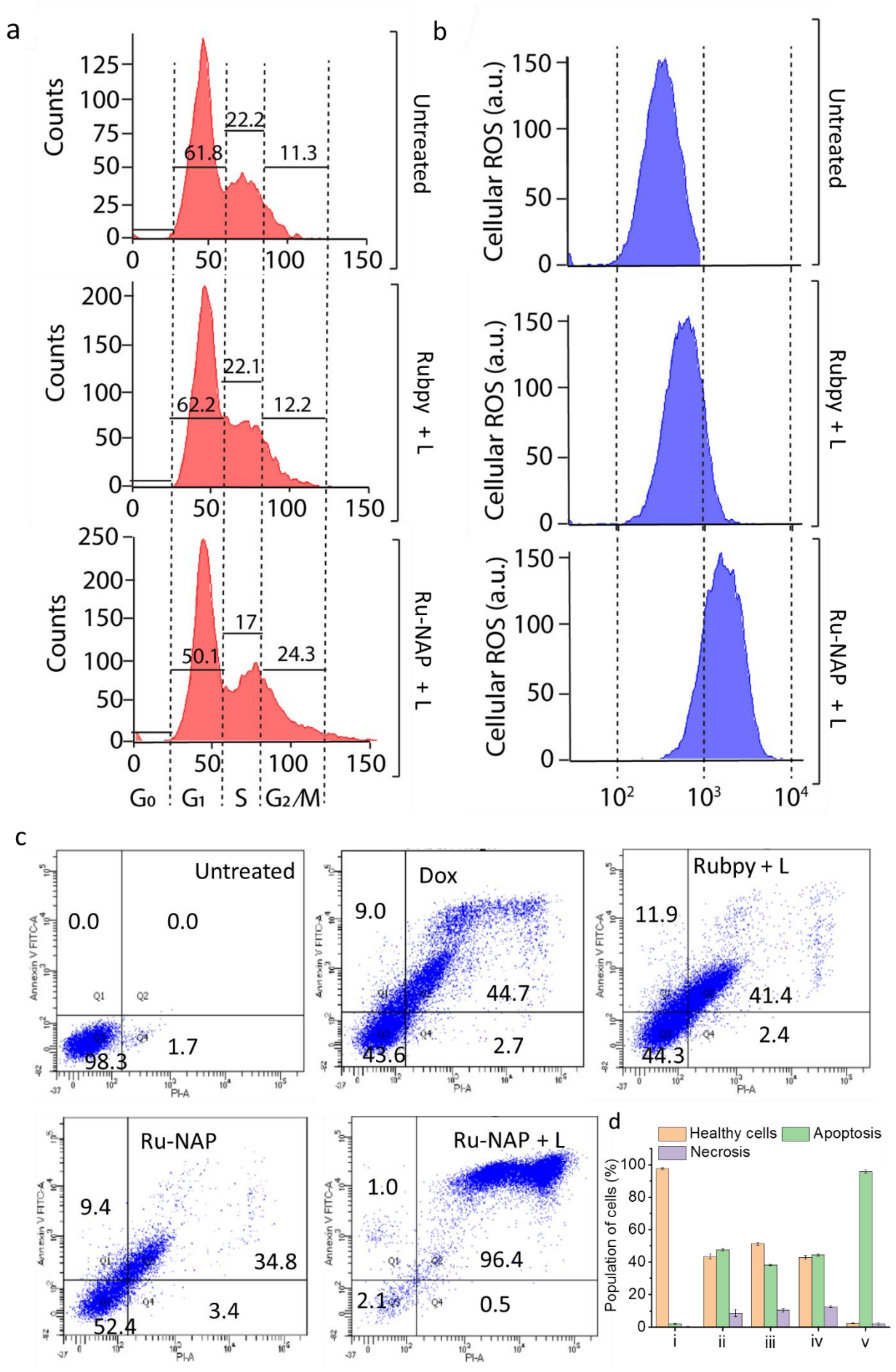
a
Counts
Untreated
61.8
22.2
11.3
Rubpy + L
62.2
22.1
12.2
Ru-NAP + L
50.1
17
24.3
G0
G1
S
G2/M
b
Cellular ROS (a.u.)
Untreated
Rubpy + L
Ru-NAP + L
c
Untreated
0.0
0.0
98.3
1.7
Dox
9.0
44.7
43.6
2.7
Rubpy + L
11.9
41.4
44.3
2.4
Ru-NAP
9.4
34.8
52.4
3.4
Ru-NAP + L
1.0
96.4
2.1
0.5
Annexin V FITC-A
PI-A
d
Healthy cells
Apoptosis
Necrosis
Population of cells (%)
i
ii
iii
iv
v

Figure 7. (a) Histograms of the distribution of DNA content by flow cytometric analyses of the **Ru-NAP** mediated cell cycle arrest. (b) Flow cytometry analysis of cellular ROS using CM-H_2DCFDA in MDA-MB231 cells, either untreated or treated with **Rubpy** or **Ru-NAP** (20 μM) separately for 4 h followed by photoactivation (450 nm, 200 mW.cm^{-2}, 5 min, 60 J.cm^{-2}). (c) Analysis of the apoptosis in flow cytometry using Dead Cell Apoptosis Kit with Annexin V Alexa Fluor™ 488 & Propidium Iodide (PI) (catalogue number: V13241) using Dox (5 μM) as a positive control. **Ru-NAP** induces apoptosis in the MDA-MB-231 cells under dark condition and after light irradiation (450 nm, 200 mW.cm^{-2}, 5 min, 60 J.cm^{-2}). (d) Histogram of percentages of healthy cells, apoptotic cells, and necrotic cells after different treatments (i: untreated, ii: Dox, iii: **Rubpy + L**, iv: **Ru-NAP**, v: **Ru-NAP + L**) in MDA-MB-231 cells, measured using flow cytometry. The data represents the mean value ± SD obtained from three independent experiments.

***In Vivo* Studies of Ru-NAP.** The PDT efficacy of the **Ru-NAP** was further verified in the *in vivo* MDA-MB-231 xenograft model in nude mice. The MDA-MB-231 cells were inoculated in the right flank of the mice. When the tumour size reached ~100 mm^3, the mice were divided into three groups with n = 5. The groups are (i) untreated, (ii) **Rubpy + L** treated and (iii) **Ru-NAP + L** treated. Mouse with the abnormal size are excluded from the study. Then the mice were treated with **Rubpy** or **Ru-NAP** (2 mg/kg per mouse) intravenously and then kept in the dark for the next 24 h followed by light irradiation for 5 min (450 nm, 200 mW.cm^{-2}, 5 min, 60 J.cm^{-2}). This was repeated every alternative day for three weeks. The tumor sizes were measured using the slide caliper and the tumor volume was calculated using the formula 0.5 x length x width^2 mm^3. The tumour size and the mice body weight were recorded every third day for three weeks. On the 21st day, each mouse was sacrificed and the tumour was isolated and the weight of each tumour was recorded. A significant decrease in the tumour sizes was observed in the **Ru-NAP+ L** treated group compared to control and **Rubpy + L** (Figure 8a). From the tumour growth ratio curve, 90% and 60% inhibition of the tumour growth was observed in three weeks for **Ru-NAP + L** and **Rubpy + L** treated group respectively compared to control (Figure 8b). There was 90.5 and 56.6% reduction in the tumour weight for **Ru-NAP + L** and **Rubpy + L** treated group, respectively, compared to control (Figure 8c). We further checked the tumor growth inhibition of **Ru-NAP** (2 mg/kg per mouse) under dark conditions using MDA-MB-231 xenograft model in nude mice with n = 5 to check the chemotherapeutic effect of the **Ru-NAP**. The tumor images and tumor growth ratio curve show 50% inhibition of the tumor growth in three weeks after Ru-NAP treatment (Figure S53). These data confirmed that **Ru-NAP** could induce tumor growth inhibition under the dark through chemotherapeutic effect and a more effective growth inhibition through MT disruption, as well as PDT induced toxicity by $^1O_2$. There was no change in the body weight of the mice after **Ru-NAP + L** and

Rubpy + L treatment compared to the control (Figure 8d). Moreover, H & E staining data of the major organs after **Ru-NAP** treatment does not show any abnormalities (Figure 8e). That indicates that **Ru-NAP** was nontoxic to the mice. The *in vivo* study further confirmed that **Ru-NAP** possessed significant tumor inhibition effect with insignificant *in vivo* toxicity.

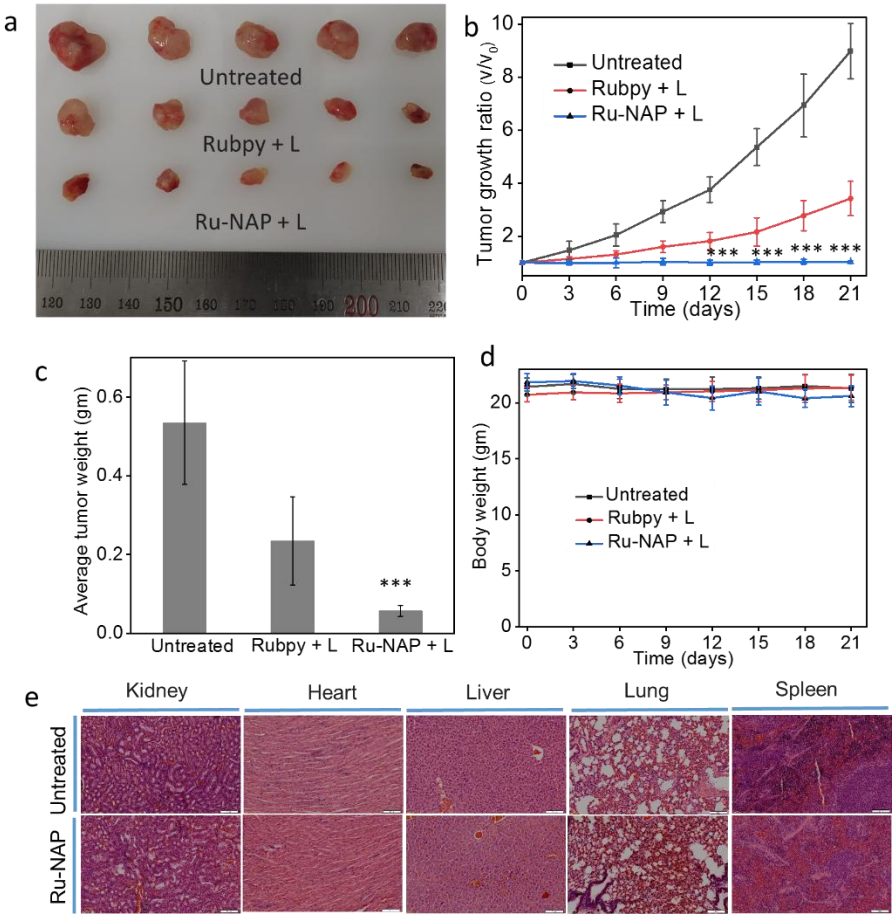

Figure 8. Tumor growth inhibition study of **Ru-NAP** followed by light irradiation (450 nm, 200 mW.cm^{-2}, 5 min, 60 J.cm^{-2}) using MDA-MB-231 tumor xenograft model in balb/c nude mice. (a) The images of the tumor of different group (n = 5) isolated from the mice at 21st day after the treatment. The result showing a significant decrease in the tumor sizes of the **Ru-NAP + L** treated group compared to untreated and **Rubpy + L**. (b) Tumor growth ratio curve of the different treatment group (n = 5). The growth ratio for the **Ru-NAP+ L** treated group is very low compared to the untreated and **Rubpy + L**. (c) Histogram of the average tumor weight of the different treatment group (n = 5) as indicated. Tumor weight is too low for **Ru-NAP + L** with respect to untreated and **Rubpy + L**. A significant difference was analysed by comparing with the non-sample-treated control group. * represents $P < 0.05$, ** represents $P < 0.01$, and *** represents $P < 0.001$. The P value was obtained using student's t-test. (d) Change in the mice bodyweight of the different treatment group (n = 5) monitored for three weeks. (e) H & E staining of the major organs (kidney, heart, liver, lung and spleen) after **Ru-NAP** treatment in nude mice showing no abnormalities indicating that **Ru-NAP** is not toxic to the mice.

Conclusion

In conclusion, we have demonstrated a proof-of-concept in developing an efficient PDT agent (**Ru-NAP**) for treating TNBC by conjugating a photoactive Ru(II)-polypyridyl moiety, efficient in generating *in-situ* $^1O_2$, to serum stable octapeptide, **NAP**. **NAP** with N-stapled termini and being a short peptide presumably evade proteolytic degradation in blood serum. The TEM images of the **Ru-NAP**/ **Py-NAP**/ **NAP**, incubated for 5 days, reveal that the fiber formation was most extensive for **Ru-NAP**, which is attributed to a favoured cation-π interaction. The metabolic stability of a short peptide, as well as its specificity in binding to the *β*-tubulin component of a matured microtubule (MT) constitute the rationale for opting for the **NAP** peptide. Specific binding to the *β*-tubulin of an *α, β*-tubulin dimer is also examined using docking studies. This confirms stronger interactions between **Ru-NAP** peptide and *β*-tubulin compared to **NAP**. Efficient binding with Ru-NAP is also established using appropriate binding studies ($K_{Ru\text{-}NAP}$: (6.8 ± 0.55) x 10^6 M^{-1} and K_{NAP}: (8.2 ± 1.1) x 10^4 M^{-1}). The average linear charge density of ~ 85 e/nm of MT further favours interaction with the cationic **Rubpy** part of a **Ru-NAP** conjugate accounts for the higher binding constant. Studies with anti-tubulin primary (EP1332Y (1:300; v/v)) and secondary antibody (ab175471, 1:500 (v/v)) with MDA-MB-231 cells, pretreated with **Ru-NAP** and followed by irradiation for 5 min (450 nm, 200 $mW.cm^{-2}$, 5 min, 60 $J.cm^{-2}$) and then incubation in dark for 20 h, revealed a noticeable change in the cell cycle profile and cell death. Tubulin polymerization assay (BK006P) confirmed that **Ru-NAP** is effective in stabilizing MT and tubulin polymerization. These account for cell death primarily through cycle arrest in G2/M phase and cell apoptosis. Apart from the *in-situ* generation of organelle-specific generation of cytotoxic $^1O_2$, fiber formation on the MT surface and /or inside the tubular structure of MT would induce an MT dysfunction and cell death. Control studies reveal that the much lower toxicity of **Ru-NAP** towards HEK293 cells compared to MDA-MB-231 cells ($^{Light}IC_{50}^{Ru\text{-}NAP}$[HEK293]: 17.2 ± 2.5 μM, compared to $^{Light}IC_{50}^{Ru\text{-}NAP}$[MDA-MB-231]: 32.5 ± 7.8 nM, $^{Dark}IC_{50}^{Ru\text{-}NAP}$[HEK293]: > 80 μM compared to $^{Dark}IC_{50}^{Ru\text{-}NAP}$[MDA-MB-231]: 2.9 ± 0.5 μM) lies in the accelerated metabolic rate of MDA-MB-231 cells as a result of the Warburg effect coupled with the accumulation of small molecules in cells once they have formed aggregates. Importantly, the Hill plot suggests a cooperative influence of fibre formation on binding to β-tubulin and $^1O_2$ generation in inducing cell death. **Ru-NAP** also shows highly effective tumour growth inhibition in the MDA-MB-

231 tumour xenograft model in nude mice. Through this report, we can establish that a new **Ru-NAP** is used effectively for treating TNBC without inducing systemic toxicity.

ASSOCIATED CONTENT

Supporting Information

The Supporting Information is available free of charge at http://

Experimental section: Peptide synthesis; Ru-NAP synthesis; characterization; Lifetime decay; docking and simulations; tryptophan quenching; DPBF and ABDA assay; lipophilicity; serum stability, morphology in cellular media; cellular uptake and endocytosis; ICP-MS; tubulin colocalization, hill plot, immunocytochemistry, western blot, cell cycle; DCFDA; annexin V/PI; *in vivo* studies

Acknowledgements: AC thanks the CSIR for a fellowship and the BOF-BILA program (BOF21BL04) of Hasselt University. AC acknowledges IISER Kolkata and Nano-biophysics and Soft Matter Interfaces Laboratory, IMO-IMOMEC, Hasselt University for the infrastructure. AD acknowledges SERB-J.C. Bose Fellowship and funding through JBR/2023/000005 grant. AD also acknowledges MoE-STARS research grant (No. 2023-47) for financial support. BJ acknowledges SERB-Ramanujan Fellowship (RJF/2022/000127) for support. BBD team is supported by SERB core research grant (CRG/2022/001322), BRNS grant (54/14/10/2022-BRNS/11014) and ICMR grant (2021-11299/CMB/ADHOC-BMS). SB acknowledges ICMR-RA Fellowship (45/35/2022-DDI/BMS).

References

(1) Risinger, A. L.; Giles, F. J.; Mooberry, S. L. Microtubule Dynamics as a Target in Oncology. *Cancer Treat. Rev*. **2009**, *35*, 255-261.

(2) Weaver, B. A. How Taxol/Paclitaxel Kills Cancer Cells. *Mol. Biol. Cell* **2014**, *25*, 2677-2681.

(3) Wang, X.; Gigant, B.; Zheng, X.; Chen. Q. Microtubule-targeting Agents for Cancer Treatment: Seven Binding Sites and Three Strategies. *Med. Comm. Oncology*. **2023**, *2*, e46.

(4) Zheng, L.; Ren, R.; Sun, X.; Zou, Y.; Shi, Y.; Di, B.; Niu, M. -M. Discovery of a Dual Tubulin and Poly (ADP-Ribose) Polymerase-1 Inhibitor by Structure-Based Pharmacophore Modeling, Virtual Screening, Molecular Docking, and Biological Evaluation. *J. Med. Chem.* **2021**, 64, *21*, 15702-15715.

(5) Shuai, W.; Wang, G.; Zhang, Y.; Bu, F.; Zhang, S.; Miller, D. D.; Li, W.; Ouyang, L.; Wang. Y. Recent Progress on Tubulin Inhibitors with Dual Targeting Capabilities for Cancer Therapy, *J. Med. Chem.* **2021**, 64, *12*, 7963-7990.

(6) Dumontet, C.; Jordan, M. A. Microtubule-binding Agents: A Dynamic Field of Cancer Therapeutics. *Nat. Rev. Drug Discov*. **2010**, *9*, 790-803.

(7) Panda, D.; Rathinasamy, K.; Santra, M. K.; Wilson, L. Kinetic Suppression of Microtubule Dynamic Instability by Griseofulvin: Implications for its Possible Use in the Treatment of Cancer. *Proc Natl Acad Sci U S A*. **2005**, *102*, 9878-9883.

(8) Honore, S., Pasquier, E.; Braguer, D. Understanding Microtubule Dynamics for Improved Cancer Therapy. *Cell. Mol. Life Sci*. **2005**, *62*, 3039-3056.

(9) Gao, L.; Meiring, J. C. M.; Varady, A.; Ruider, I. E.; Heise, C.; Wranik, M.; Velasco, C. D.; Taylor, J. A.; Terni, B.; Weinert, T.; Standfuss, J.; Cabernard, C. C.; Llobet, A.; Steinmetz, M. O.; Bausch, A. R.; Distel, M.; Thorn-Seshold, J.; Akhmanova, A.; Thorn-Seshold, O. In Vivo Photocontrol of Microtubule Dynamics and Integrity, Migration and Mitosis, by The Potent GFP-Imaging-Compatible Photoswitchable Reagents SBTubA4P and SBTub2M. *J. Am. Chem. Soc*. **2022**, *144*, 5614-5628.

(10) Klute, K.; Nackos, E.; Tasaki, S.; Nguyen, D. P.; Bander, N. H.; Tagawa, S.T. Microtubule Inhibitor-based Antibody-drug Conjugates for Cancer Therapy. *Onco Targets Ther*. **2014**, *7*, 2227-2236.

(11) Mukhtar, E.; Adhami, V. M.; Mukhtar, H. Targeting Microtubules by Natural Agents for Cancer Therapy. *Mol Cancer Ther*. **2014**, *13*, 275-284.

(12) Jordan, M. A.; Wilson, L. Microtubules as a Target for Anticancer Drugs. *Nat. Rev. Cancer*. **2004**, *4*, 253-265.

(13) Shuai, W.; Wang, G.; Zhang, Y.; Bu, F.; Zhang, S.; Miller, D. D.; Li, W.; Ouyang, L.; Wang, Y. Recent Progress on Tubulin Inhibitors with Dual Targeting Capabilities for Cancer Therapy. *J. Med. Chem*. **2021**, *64*, 7963-7990.

(14) Pérez-Pérez, M. J.; Priego, E. M.; Bueno, O.; Martins, M. S.; Canela, M. D.; Liekens, S. Blocking Blood Flow to Solid Tumors by Destabilizing Tubulin: an Approach to Targeting Tumor Growth. *J. Med. Chem*. **2016**, *59*, 8685-8711.

(15) Greene, L. M.; Meegan, M. J.; Zisterer, D. M. Combretastatins: More than just Vascular Targeting Agents? *J. Pharmacol. Exp. Ther*. **2015**, *355*, 212-227.

(16) Xiao, H.; Verdier-Pinard, P.; Fernandez-Fuentes, N.; Burd, B.; Angeletti, R.; Fiser, A.; Horwitz, S. B.; Orr, G. A. Insights into the Mechanism of Microtubule Stabilization by Taxol. *Proc Natl Acad Sci U S A*. **2006**, *103*, 10166-10173.

(17) Markman, M. Antineoplastic Agents in the Management of Ovarian Cancer: Current Status and Emerging Therapeutic Strategies. *Trends Pharmacol. Sci*. **2008**, *29*, 515-519.

(18) Sharifi-Rad, J.; Quispe, C.; Patra, J. K.; Singh, Y. D.; Panda, M. K.; Das, G.; Adetunji, C.O.; Michael, O. S.; Sytar, O.; Polito, L.; Živković, J.; Cruz-Martins, N.; Klimek-Szczykutowicz, M.; Ekiert, H.; Choudhary, M. I.; Ayatollahi, S. A.; Tynybekov, B.; Kobarfard, F.; Muntean, A. C.; Grozea, I.; Daştan, S. D.; Butnariu, M.; Szopa, A.; Calina, D. Paclitaxel: Application in Modern Oncology and Nanomedicine-Based Cancer Therapy. *Oxid. Med. Cell. Longev*. **2021**, 3687700.

(19) Rohena, C. C.; Mooberry, S. L. Recent Progress with Microtubule Stabilizers: New Compounds, Binding Modes and Cellular Activities. *Nat. Prod. Rep*. **2014**, *31*, 335-355.

(20) Rixel, V. H. S. V.; Ramu, V.; Auyeung, A. B.; Beztsinna, N.; Leger, D. Y.; Lameijer, L. N.; Hilt, S. T.; Dévédec, S. E. L.; Yildiz, T.; Betancourt, T.; Gildner, M. B.; Hudnall, T. W.; Sol, V.; Liagre, B.; Kornienko, A.; Bonnet. S. Photo-Uncaging of a Microtubule-Targeted Rigidin Analogue in Hypoxic Cancer Cells and in a Xenograft Mouse Model. *J. Am. Chem. Soc*. **2019**, *141*, 18444-18454.

(21) Divinski, I.; Holtser-Cochav, M.; Vulih-Schultzman, I.; Steingart, R. A.; Gozes, I. Peptide Neuroprotection through Specific Interaction with Brain Tubulin. *J. Neurochem*. **2006**, *98*, 973-984.

(22) Oz, S.; Kapitansky, O.; Ivashco-Pachima, Y.; Malishkevich, A.; Giladi, E.; Skalka, N.; Rosin-Arbesfeld, R.; Mittelman, L.; Segev, O.; Hirsch, J. A.; Gozes, I. The NAP Motif of Activity-Dependent Neuroprotective Protein (ADNP) Regulates Dendritic Spines through Microtubule End Binding Proteins. *Mol. Psychiatry*. **2014**, *19*, 1115-1124.

(23) Li, Y.; Zhang, H.; Merkher, Y. Recent Advances in Therapeutic Strategies for Triple-Negative Breast Cancer. *J. Hematol. Oncol*. **2022**, *15*, 121.

(24) Bulina, M. E.; Lukyanov, K. A.; Britanova, O. V. Onichtchouk, D.; Lukyanov, S.; Chudakov, D. M. Chromophore-Assisted Light Inactivation (CALI) using the Phototoxic Fluorescent Protein KillerRed *Nat Protoc*. **2006**, *1*, 947-953.

(25) Zhang, L.; Wang, P.; Zhou, X-Q.; Bretin, L.; Zeng, X.; Husiev, Y.; Polanco, E. A.; Zhao, G.; Wijaya, L. S.; Biver, T.; Le Dévédec, S. E.; Sun, W.; Bonnet, S. Cyclic Ruthenium-Peptide Conjugates as Integrin-Targeting Phototherapeutic Prodrugs for the Treatment of Brain Tumors. *J. Am. Chem. Soc*. **2023**, *145*, 14963-14980.

(26) Cole, H. D.; Vali, A.; Roque, J. A.; Shi, G.; Kaur, G.; Hodges, R. O.; Francés-Monerris, A.; Alberto, M. E.; Cameron, C. G.; McFarland, S. A. Ru (II) Phenanthroline-Based Oligothienyl Complexes as Phototherapy Agents. *Inorg. Chem*. **2024**, *63*, 11450-11458.

(27) Burke, C. S.; Byrne, A.; Keyes, T. E. Targeting Photoinduced DNA Destruction by Ru(II) Tetraazaphenanthrene in Live Cells by Signal Peptide. *J. Am. Chem. Soc*. **2018**, *140*, 6945-6955.

(28) Chakrabortty, S.; Agrawalla, B. K.; Stumper, A.; Vegi, N. M.; Fischer, S.; Reichardt, C.; Kögler, M.; Dietzek, B.; Feuring-Buske, M.; Buske, C.; Rau, S.; Weil, T. Mitochondria Targeted Protein-Ruthenium Photosensitizer for Efficient Photodynamic Applications. *J. Am. Chem. Soc*. **2017**, *139*, 2512-2519.

(29) Jacobson, K.; Rajfur, Z.; Vitriol, E.; Hahn, K. Chromophore-Assisted Laser Inactivation in Cell Biology. *Trends Cell Biol.* **2008**, *18*, 443-450.

(30) Ogorek, A. N.; Zhou, X.; Martell, J. D. Switchable DNA Catalysts for Proximity Labeling at Sites of Protein-Protein Interactions. *J. Am. Chem. Soc*. **2023**, *145*, 16913-16923.

(31) Sato, S.; Morita, K.; Nakamura, H. Regulation of Target Protein Knockdown and Labeling Using Ligand-Directed $Ru(bpy)_3$ Photocatalyst. *Bioconjugate Chem*. **2015**, 26, 250-256.

(32) Takemoto, K.; Iwanari, H.; Tada, H.; Suyama, K.; Sano, A.; Nagai, T.; Hamakubo, T.; Takahashi, T. Optical Inactivation of Synaptic AMPA Receptors Erases Fear Memory. Nat. Biotechnol. 2017, 35, 38-47.

(33) Robert A. Hill1, R. A.; Eyiyemisi C. Damisah, E. C.; Chen, F.; Alex C. Kwan, A. C.; Grutzendler, J. Targeted Two-Photon Chemical Apoptotic Ablation of Defined Cell Types in Vivo. *Nat. Commun*. **2017**, *8*, 15837.

(34) Fu, Z.; Li, S.; Han, S. Antibody Drug Conjugate: the “Biological Missile” for Targeted Cancer Therapy. *Signal Transduct. Target Ther.* 2022, *7*, 93.

(35) Beck, A.; Goetsch, L.; Dumontet. C.; Corvaïa, N. Strategies and Challenges for the Next Generation of Antibody-Drug Conjugates. *Nat. Rev. Drug Discov*. **2017**, *16*, 315-337.

(36) Acharya, S.; Maji, M.; Chakraborty, M. P.; Bhattacharya, I.; Das, R.; Gupta, A.; Mukherjee, A. Disruption of the Microtubule Network and Inhibition of VEGFR2 Phosphorylation by Cytotoxic N,O-Coordinated Pt(II) and Ru(II) Complexes of Trimethoxy Aniline-Based Schiff Bases. *Inorg. Chem*. **2021**, *60*, 3418-3430.

(37) Adak, A.; Mohapatra, S.; Mondal, P.; Jana, B.; Ghosh, S. Design of a Novel Microtubule Targeted Peptide Vesicle for Delivering Different Anticancer Drugs. *Chem. Commun.* **2016**, *52*, 7549-7552.

(38) Gong, L.; Zhao, H.; Liu, Y.; Wu, H.; Liu, C.; Chang, S.; Chen, L.; Jin, M.; Wang, Q.; Gao, Z.; Huang, W. Research Advances in Peptide-Drug Conjugates. *Acta Pharm. Sin. B*. **2023**, *13*, 3659-3677.

(39) Rizvi, S. F. A.; Zhang, L.; Zhang, H.; Fang, Q. Peptide-Drug Conjugates: Design, Chemistry, and Drug Delivery System as a Novel Cancer Theranostic. *ACS Pharmacol. Transl. Sci*. **2024**, *7*, 309-334.

(40) Plaetzer, K.; Krammer, B.; Berlanda, J.; Berr, F.; Kiesslich, T. Photophysics and photochemistry of photodynamic therapy: fundamental aspects. *Lasers. Med. Sci*. **2009**, *24*, 259-268.

(41) Ghosh, H.N.; Das, A. Advances in Inorganic Chemistry (Academic Press-ELSEVIER), **2023**, *81*, 305-344.

(42) Yi, X.; Dai, J.; Han, Y.; Xu, M.; Zhang. X; Zhen, S.; Zhao; Z.; Lou, X.; Xia, F. A high therapeutic efficacy of polymeric prodrug nano-assembly for a combination of photodynamic therapy and chemotherapy. *Commun. Biol*. **2018**, *1*, 1-13.

(43) Bretin, L.; Husiev, Y.; Ramu, V.; Zhang, L.; Hakkennes, M.; Abyar, S.; Johns, A. C.; Dévédec, S.E.L.; Betancourt, T.; Kornienko, A.; Bonnet, S. Red-Light Activation of a Microtubule Polymerization Inhibitor via Amide Functionalization of the Ruthenium Photocage. *Angew. Chem. Int. Ed*. **2024**, *63*, e202316425.

(44) Cao, F.; Wang, H.; Lu, N.; Zhang, P.; Huang, H. A Photoisomerizable Zinc (II) Complex Inhibits Microtubule Polymerization for Photoactive Therapy. *Angew. Chem. Int. Ed*. **2023**, *62*, e202301344.

(45) Schmitt, C.; Mauker, P.; Vepřek, N. A.; Gierse, C.; Meiring, J. C. M.; Kuch, J.; Akhmanova, A.; Dehmelt, L.; Thorn-Seshold, O. A Photocaged Microtubule-Stabilising Epothilone Allows Spatiotemporal Control of Cytoskeletal Dynamics. *Angew. Chem. Int. Ed*. **2024**, *63*, e202410169.

(46) Sailer, A.; Meiring, J. C. M.; Heise, C.; Pettersson, L. N.; Akhmanova, A.; Thorn-Seshold, J.; Thorn-Seshold, O. Pyrrole Hemithioindigo Antimitotics with Near-Quantitative Bidirectional Photoswitching that Photocontrol Cellular Microtubule Dynamics with Single-Cell Precision. *Angew. Chem. Int. Ed*. **2021**, *60*, 23695

(47) E. Elgar, C. E.; Yusoh, N. A.; Tiley, P. R.; Kolozsvári, N.; Bennett, L. G.; Gamble, A.; Péan, E. V.; Davies, M. L.; Staples, C. J.; Ahmad, H.; Gill, M. R. Ruthenium (II) Polypyridyl Complexes as FRET Donors: Structure-and Sequence-Selective DNA-Binding and Anticancer Properties. *J. Am. Chem. Soc.* **2023**, *145*, 1236-1246.

(48) B J.; Zhang, Y.; Wu1, S.; Li, H.; Sun, L.; Liu, Y.; Zhu, X.; Qiao, X.; Ma, Q.; Liu, C.; Niu, N.; Xue, J.; Chen, G.; Yang, Y.; Liu, C. KK-LC-1 as a Therapeutic Target to Eliminate $ALDH^{+}$ Stem Cells in Triple Negative Breast Cancer. *Nat. Commun*. **2023**, *14*, 2602.

(49) Maisch, T.; Baier, J.; Franz, B.; Bäumler, W. The Role of Singlet Oxygen and Oxygen Concentration in Photodynamic Inactivation of Bacteria. *Proc. Natl. Acad. Sci. U S A.* **2007**, *104*, 7223-7228.

(50) Carbonaro, M.; Escuin, D.; O'Brate, A.; Thadani-Mulero, M.; Giannakakou, P. Microtubules Regulate Hypoxia-inducible Factor-1α Protein Trafficking and Activity. *J. Biol. Chem*. **2012**, *287*, 11859-11869.

(51) Raza, A.; Archer, S. A.; Fairbanks, S. D.; Smitten, K. L.; Botchway, S. W.; Thomas, J.A.; MacNeil, S.; Haycock, J. W. A Dinuclear Ruthenium (II) Complex Excited by Near-Infrared Light through Two-Photon Absorption Induces Phototoxicity Deep within Hypoxic Regions of Melanoma Cancer Spheroids. *J. Am. Chem. Soc***. 2020**, *142*, 4639-4647.

(52) Heinemann, F.; Karges, J.; Gasser, G. Critical Overview of the Use of Ru(II) Polypyridyl Complexes as Photosensitizers in One-Photon and Two-Photon Photodynamic Therapy. *Acc. Chem. Res*. **2017**, *50*, 2727-2736.

(53) Li, X.; Kwon, N.; Guo, T.; Liu, Z.; Yoon, J. Innovative Strategies for Hypoxic-Tumor Photodynamic Therapy. *Angew. Chem. Int. Ed*. **2018**, *57*, 11522-11531.

(54) Ghosh, A.; Das, P.; Gill, M. R.; Kar, P.; Walker, M. G.; Thomas, J. A.; Das, A. Photoactive Ru^{II}-Polypyridyl Complexes that Display Sequence Selectivity and High-Affinity Binding to Duplex DNA through Groove Binding. *Chem. Eur. J*. **2011**, *17*, 2089-2098.

(55) Poynton, F. E.; Bright, S.A.; Blasco, S.; Williams, D. C.; Kelly, J. M.; Gunnlaugsson, T. The Development of Ruthenium (II) Polypyridyl Complexes and Conjugates for in Vitro Cellular and in Vivo Applications. *Chem. Soc. Rev*. **2017**, *46*, 7706-7756.

(56) Bonnet, S. Ruthenium-Based Photoactivated Chemotherapy. *J. Am. Chem. Soc*. **2023**, *145*, 23397-23415.

(57) Goodson, H. V.; Jonasson, E. M. Microtubules and Microtubule-Associated Proteins. *Cold Spring Harb. Perspect. Biol.* **2018**, *10*, a022608.

(58) Sekulić, D. L.; Satarić, M. V. An Improved Nanoscale Transmission Line Model of Microtubule: The Effect of Nonlinearity on the Propagation of Electrical Signals. *Elec. Energ*. **2015**, *28*, 133-142.

(59) Minoura, I.; Muto, E. Dielectric Measurement of Individual Microtubules Using the Electroorientation Method. *Biophys. J*. **2006**, *90*, 3739-3748.

(60) Adak, A.; Das, G.; Barman, S.; Mohapatra, S.; Bhunia, D.; Jana, B.; Ghosh, S. Biodegradable Neuro-Compatible Peptide Hydrogel Promotes Neurite Outgrowth, Shows Significant Neuroprotection, and Delivers Anti-Alzheimer Drug. *ACS Appl. Mater. Interfaces*. **2017**, *9*, 5067-5076.

(61) Pierce, S.; Jennings, M. P.; Juliano, S. A.; Angeles-Boza, A. M. Peptide-Ruthenium Conjugate as an Efficient Photosensitizer for the Inactivation of Multidrug-Resistant Bacteria. *Inorg. Chem*. **2020**, *59*, 14866-14870.

(62) Kandoth, N.; Chaudhary, S.; Gupta, S.; Raksha, K.; Chatterjee, A.; Gupta, S.; Karuthedath, S.; Castro, C. D.; Laquai, F.; Pramanik, S. K.; Bhattacharyya, S.; Mallick, A. I.; Das, A.

Multimodal Biofilm Inactivation Using a Photocatalytic Bismuth Perovskite-TiO_2-Ru(II)polypyridyl-Based Multisite Heterojunction. *ACS Nano*, **2023**, *17*, 10393-10406.

(63) Banerjee, T.; Rawalekar, S.; Das, A.; Ghosh, H. N. Interfacial Electron Transfer Dynamics of Two Newly Synthesized Catecholate Bound Ru^{II} Polypyridyl-Based Sensitizers on TiO_2 Nanoparticle Surface-A Femtosecond Pump Probe Spectroscopic Study. *Eur. J. Inorg. Chem*. **2011**, 4187-4197.

(64) Mahato, P.; Saha, S.; Choudhury, S.; Das, A. Solvent-Dependent Aggregation Behavior of a New Ru (II)-Polypyridyl Based Metallo surfactant. *Chem. Commun.* **2011**, *47*, 11074-11076.

(65) Zhang, K. Y.; Yu, Q.; Wei, H.; Liu, S.; Zhao, Q.; Huang, W. Long-Lived Emissive Probes for Time-Resolved Photoluminescence Bioimaging and Biosensing *Chem. Rev*. **2018**, *118*, 1770-1839.

(66) Shum, J.; Leung, P. K-K.; Lo, K. K-W. Luminescent Ruthenium (II) Polypyridine Complexes for a Wide Variety of Biomolecular and Cellular Applications. *Inorg. Chem*. **2019**, *58*, 2231-2247.

(67) Byrne, A.; Burkeab, C. S.; Keyes, T. E. Precision Targeted Ruthenium (II) Luminophores; Highly Effective Probes for Cell Imaging by Stimulated Emission Depletion (STED) Microscopy. *Chem. Sci.* **2016**, *7*, 6551-6562.

(68) Martin, A.; Byrne, A.; Burke, C. S.; Forster, R. J.; Keyes, T. E. Peptide-Bridged Dinuclear Ru (II) Complex for Mitochondrial Targeted Monitoring of Dynamic Changes to Oxygen Concentration and ROS Generation in Live Mammalian Cells. *J. Am. Chem. Soc*. **2014**, *136*, 15300-15309.

(69) Gozes, I.; Morimoto, B. H.; Tiong, J.; Fox, A.; Sutherland, K.; Dangoor, D.; Holser-Cochav, M.; Vered, K.; Newton, P.; Aisen, P. S.; Matsuoka, Y.; Dyck, C. H. V.; Thal, L. NAP: Research and Development of a Peptide Derived from Activity-Dependent Neuroprotective Protein (ADNP). *CNS Drug Rev*. **2005**, *11*, 353-368.

(70) Yammine, A.; Gao, J.; Kwan, A. H. Tryptophan Fluorescence Quenching Assays for Measuring Protein-ligand Binding Affinities: Principles and a Practical Guide. *Bio Protoc.* **2019**, *9*, e3253.

(71) Chakraborti, S.; Das, L.; Kapoor, A. N.; Dwivedi, V.; Poddar, A.; Chakraborti, G.; Janik, M.; Basu, G.; Panda, D.; Chakrabarti, P.; Surolia, A.; Bhattacharyya, B. Curcumin Recognizes a Unique Binding Site of Tubulin. *J. Med. Chem.* **2011**, *54*, 6183-6196.

(72) Jana, B.; Mohapatra, S.; Mondal, P.; Barman, S.; Pradhan, K.; Saha, A.; Ghosh, A. α-Cyclodextrin Interacts Close to Vinblastine Site of Tubulin and Delivers Curcumin Preferentially to the Tubulin Surface of Cancer Cell. *ACS Appl. Mater. Interfaces*. **2016**, *8*, 13793-13803.

(73) Gupta, K.; Panda, D. Perturbation of Microtubule Polymerization by Quercetin through Tubulin Binding: A Novel Mechanism of its Antiproliferative Activity. *Biochemistry*. **2002**, *41*, 13029-13038.

(74) Biswas, A.; Kurkute, P.; Jana, B.; Laskar, A.; Ghosh, S. An Amyloid Inhibitor Octapeptide forms Amyloid Type Fibrous Aggregates and Affects Microtubule Motility. *Chem. Commun*. **2014**, *50*, 2604-2607.

(75) Ashur-Fabian, O.; Segal-Ruder, Y.; Skutelsky, E.; Brenneman, D. E.; Steingart, R. A.; Giladi, E.; Gozes; I. The Neuroprotective Peptide NAP Inhibits the Aggregation of the Beta-Amyloid Peptide. *Peptides*. **2003**, *24*, 1413-1423.

(76) Przybyla, D. E.; Chmielewski, J. Metal-Triggered Radial Self-Assembly of Collagen Peptide fibers. *J. Am. Chem. Soc*. **2008**, *130*, 12610-12611.

(77) Entradas, T.; Waldrona, S.; Volk, M. The Detection Sensitivity of Commonly Used Singlet Oxygen Probes in Aqueous Environments. *J. Photochem. Photobiol. B*. **2020**, *204*, 111787.

(78) Lindig, B. A.; Rodgers, M. A. J.; Paul Schaap, A. Determination of the Lifetime of Singlet Oxygen in D_2O Using 9,10-Anthracenedipropionic Acid, a Water-Soluble Probe. J. Am. Chem. Soc. 1980, 102, 5590-5593.

(79) Ramu, V.; Aute, S.; Taye, N.; Guha, R.; Walker, M. G.; Mogare, D.; Parulekar, A.; Thomas, J. A.; Chattopadhyay, S.; Das, A. Photo-Induced Cytotoxicity and Anti-Metastatic Activity of Ruthenium(II)-Polypyridyl Complexes Functionalized with Tyrosine or Tryptophan. *Dalton Trans*. **2017**, *46*, 6634-6644.

(80) Han, G.; Li, G.; Huang, J.; Han, C.; Turro, C.; Sun, Y. Two-Photon-Absorbing Ruthenium Complexes Enable Near Infrared Light-Driven Photocatalysis. *Nat. Commun*. **2022**, *13*, 2288.

(81) Toupin, N.; Steinke, S. J.; Nadella, S.; Li, A.; Rohrabaugh, T. N.; Samuels, E. R.; Turro, C.; Sevrioukova, I. F.; Kodanko, J. J. Photosensitive Ru(II) Complexes as Inhibitors of the Major Human Drug Metabolizing Enzyme CYP3A4. *J.Am. Chem. Soc.*, **2021**, *143*, 9191-9205.

(82) Acharya, S.; Maji, M.; Chakraborty, M. P.; Bhattacharya, I.; Das, R.; Gupta, A.; Mukherjee, A. Disruption of Microtubule Network and Inhibition of VEGFR2 Phosphorylation by Cytotoxic N,O Coordinated Pt(II) and Ru(II) Complexes of Trimethoxy Aniline Based Schiff Bases. *Inorg. Chem*. **2021**, *60*, 3418-3430.

(83) Poynton, F. E.; Bright, S. A.; Blasco, S.; Williams, D. C.; Kelly, J. M.; Gunnlaugsson, T. The Development of Ruthenium(II) Polypyridyl Complexes and Conjugates for *in Vitro* Cellular and *in Vivo* Applications. *Chem. Soc. Rev.*, **2017**, *46*, 7706-7756.

(84) H. van Rijt, S.; Mukherjee, A.; Pizarro, A. M.; Sadler, P. J. Cytotoxicity, Hydrophobicity, Uptake, and Distribution of Osmium(II) Anticancer Complexes in Ovarian Cancer Cells. *J. Med. Chem*. **2010**, 53, 840-849.

(85) Zhang, R.; Qin, X.; Kong, F.; Chen, P.; Pan, G. Improving Cellular Uptake of Therapeutic Entities through Interaction with Components of Cell Membrane. *Drug Deliv*. **2019**, *26*, 328-342.

(86) Mitchell, M. J.; Billingsley, M. M.; Haley, Wechsler, M. E.; Peppas, N. A.; Langer, R. Engineering Precision Nanoparticles for Drug Delivery. *Nat. Rev. Drug Discov*. **2021**, *20*, 101-124.

(87) Bhargava, S.; Kulkarni, R.; Dewangan, B.; Jiaswar, C.; Kumar, K.; Kumar, A.; Kulkarni, N.; Bodhe, P. R.; Kumarb, H.; Sahu, B. Microtubule Stabilising Peptides: New Paradigm towards Management of Neuronal Disorders. *RSC Med. Chem*. **2023**, *14*, 2192-2205.

(88) Silva, S.; Almeida, A. J.; Vale, N. Combination of Cell-Penetrating Peptides with Nanoparticles for Therapeutic Application: A Review. *Biomol*. **2019**, *9*, 22.

(89) Liu, K.; Newbury, P. A.; Glicksberg, B.S.; Zeng, W. Z. D.; Paithankar, S.; Andrechek, E. R.; Chen, B. Evaluating Cell Lines as Models for Metastatic Breast Cancer through Integrative Analysis of Genomic Data. *Nat. Commun*. **2019**, *10*, 2138.

(90) Gao, Y.; Shi, J.; Yuan, D.; Xu, B. Imaging Enzyme-Triggered Self-Assembly of Small Molecules inside Live Cells. *Nat. Commun*. **2012**, *3*, 1033.

(91) Bigman, L. S.; Levy, Y. Protein Diffusion on Charged Biopolymers: DNA Versus Microtubule. *Biophys. J*. **2020**, *118*, 3008-3018.

(92) Hsu, P. P.; Sabatini, D. M. Cancer Cell Metabolism: Warburg and Beyond. *Cell*. **2008**, *134*, 703-707.

(93) Yang, Z. M.; Liang, G. L.; Guo, Z. F.; Guo, Z. H.; Xu, B. Intracellular Hydrogelation of Small Molecules Inhibits Bacterial Growth. *Angew. Chem. Int. Ed*. **2007**, *46*, 8216-8219.

(94) Kuang, Y.; Xu, B. Disruption of the Dynamics of Microtubules and Selective Inhibition of Glioblastoma Cells by Nanofibers of Small Hydrophobic Molecules. *Angew. Chem. Int. Ed.* **2013**, *52*, 6944-6948.

(95) D'Amato, A.; Mariconda, A.; Iacopetta, D.; Ceramella, J.; Catalano, A.; Sinicropi, M.S.; Longo, P. Complexes of Ruthenium(II) as Promising Dual-Active Agents against Cancer and Viral Infections. *Pharmaceuticals*. **2023**, *16*, 1729.

(96) Verlato, G.; Cerveri, I.; Villani, A.; Pasquetto, M.; Ferrari, M.; Fanfulla, F.; Zanolin, E.; Rijcken, B.; Marco, R. Evaluation of Methacholine Dose-Response Curves by Linear and Exponential Mathematical Models: Goodness-of-Fit and Validity of Extrapolation. *Eur. Respir. J*. **1996**, *9*, 506-511.

(97) Wang, C., Huang, S. -B., Yang, M. -C., Lin, Y. -T., Chu, I. -H., Shen, Y. -N., Chiu, Y. -H., Hung, S. -H., Kang, L., Hong, Y. -R. Combining Paclitaxel with ABT-263 Has a Synergistic Effect on Paclitaxel Resistant Prostate Cancer Cells. *PLoS One.* **2015**, *10*, e0120913.

(98) De, K. Decapeptide Modified Doxorubicin Loaded Solid Lipid Nanoparticles as Targeted Drug Delivery System against Prostate Cancer *Langmuir***. 2021**, *37*, 13194-13207.

(99) Sarkar, S.; Chatterjee, A.; Kim, D.; Saritha, C.; Barman, S.; Jana, B.; Ryu, J-H.; Das, A. Host-Guest Adduct as a Stimuli-responsive Prodrug: Enzyme-Triggered Self-Assembly Process of a Short Peptide within Mitochondria to Induce Cell Apoptosis. *Adv Healthcare Mater*. **2024**, 2403243.

ToC:

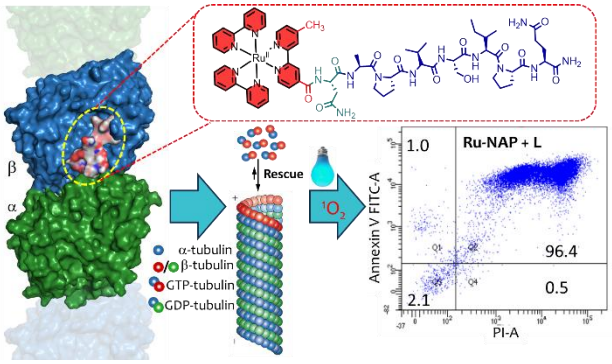

An efficient bimodal photodynamic therapeutic agent composed of an octapeptide (**NAP**) with N-stapled termini through a carboxylic acid derivative of a photoactive Ru(2,2'-bipy)$_3^{2+}$ (**Rubpy**) complex (**Ru-NAP**) is designed for treating Triple-Negative Breast Cancer (TNBC). Specific binding of the serum-stable **Ru-NAP** to the E-site of the β^{III}-tubulin favours polymerization and induces dynamic instability of the microtubule. These lead to G2/M cell cycle arrest, effective generation of *in situ* singlet oxygen ($^1O_2$, Type II ROS) through photo-activation and apoptotic death with significant tumor growth inhibition.